NASA-CR-193206

P. 46

SYSTEMS ANALYSIS ON LASER BEAMED POWER

April, 1993

Prepared by:

Dr. Glenn W. Zeiders Jr.

The Sirius Group
227 Bartholomew Street
Peabody, Massachusetts 01960

Prepared for:

National Aeronautics and Space Administration

George C. Marshall Space Flight Center

Marshall Space Flight Center, AL 35812

under

NASA Contract H-11986D

SYSTEMS ANALYSIS ON LASER BEAMED POWER

April, 1993

Prepared by:
Dr. Glenn W. Zeiders Jr.

The Sirius Group
227 Bartholomew Street
Peabody, Massachusetts 01960

Prepared for:

National Aeronautics and Space Administration

George C. Marshall Space Flight Center

Marshall Space Flight Center, AL 35812

under

NASA Contract H-11986D

National Aeronautics and
Space Administration

NASA

George C. Marshall Space Flight Center
Marshall Space Flight Center, Alabama
35812

Reply to Attn of: PS04

May 13, 1993

TO: Distribution

FROM: PS04/Sandy Montgomery

SUBJECT: Final Report "Systems Analysis on Laser Beamed Power"

Please find attached a copy of the subject report submitted by Glenn
Zeiders of the Sirius Group. It covers activities performed under
contract to MSFC in 1992. The analysis is related to the Space Laser
Energy (SELENE) program, for which MSFC is the lead center. It is an
excellent compendium and analysis of the technical issues facing the
program. Comments may be addressed to myself or Glenn Zeiders at the
given address.. If necessary, you may contact me at (205) 544-1767.

Sandy Montgomery
Orbital Support Systems

SYSTEMS ANALYSIS ON LASER BEAMED POWER

CONTRACT: H-11986D   1-2-PP-02176 (1F)   Value: $25000
Period of Performance: 11 May 92 - 10 Oct 92

CONTRACTOR: The Sirius Group
227 Bartholomew Street
Peabody, Massachusetts 01960

TECH. MANAGER: E. E. Montgomery, IV, PS04
National Aeronautics and Space Administration
George C. Marshall Space Flight Center
Marshall Space Flight Center, AL 35812
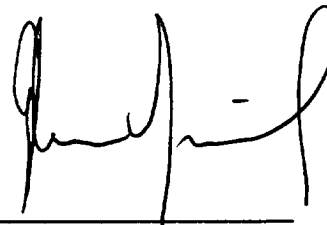
STATEMENT OF WORK:

Provide systems analysis on laser beamed power systems suitable for transmitting power from ground to space. Analyses shall include overall systems trades including cost, schedule, and system performance implications as applicable. The analyses to be done shall be jointly selected by the contractor and MSFC, and shall supplement work previously done.

Assess the status of related technology work in progress on laser and optical components/subsystems and provide recommendations for future work.

Provide analyses, data, and recommendations supportive of cooperative activities and related systems.

Develop system descriptions for alternative concepts. These descriptions are to include block diagrams with accompanying text. Also provide summary conclusions from review of project trade studies and provide recommendations for future activities.

Attend meetings at MSFC and at other locations, providing consultation related to this effort. Provide parametric sensitivity data and other supporting data periodically, and a report at the end of the work. Provide documentation in electronic form (Macintosh preferred) and in paper format.

Dr. Glenn W. Zeiders Jr.,
The Sirius Group

Technical Considerations and Recommendations for SELENE

Originally conceived for the purpose of delivering power to a lunar station during the 14-day lunar night, the SELENE program during the past year evolved into a far more significant one for long-term NASA interests as it became apparent that the system could also

- supply the power for the orbital transfer vehicles needed to economically transfer materials and personnel from LEO to space platforms, lunar stations, and beyond, both to establish them in the first place and thereafter to sustain them, and
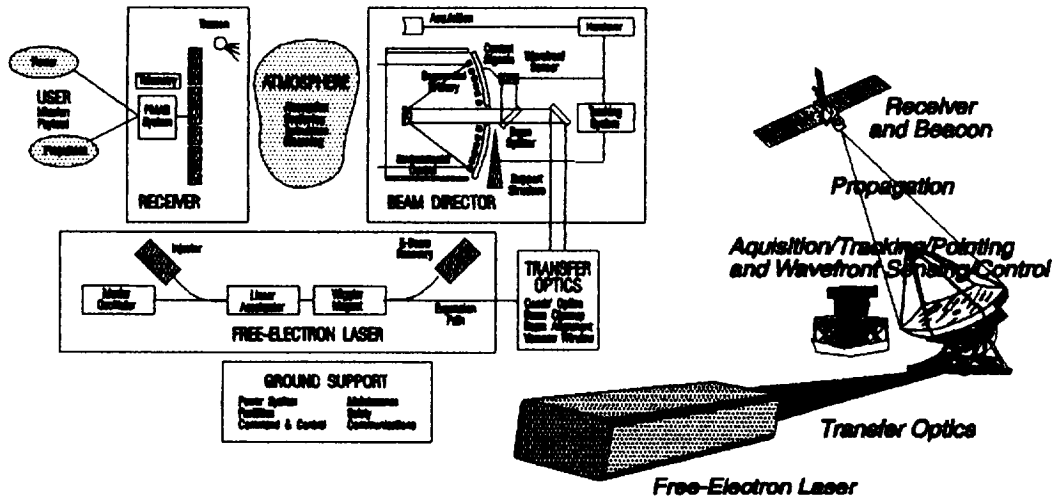- augment or replace new satellite power and propulsion systems and regenerate aging high-value satellites.

Fig. 1 Laser Power Beaming Elements

The primary elements of a laser power beaming system required to satisfy these applications -- surface, transportation., and satellite -- are shown in Fig. 1. Although the elements can be separately identified and developed, there is a strong interplay between them, and this report will attempt to look at them as a whole and to make recommendations for the future. *The views expressed here are those of the author, and do not necessarily represent those of NASA or of any of its other contractors.*

The two most important factors driving the configuration of the power beaming system have been (1) minimization of weight in space because of the extremely high costs associated with it and (2) the continued use of photovoltaic conversion with solar cells so that the receivers can function with both solar and laser power. The spectral response characteristics for the major types of available cells are shown in Fig. 2 from which it can be seen that the high efficiencies required to minimize weight in space will recommend operation with GaAs in the 0.8 - 0.85 μ range. Silicon is the most widely-used material today, and it is expected that radiation damage will move its response peak
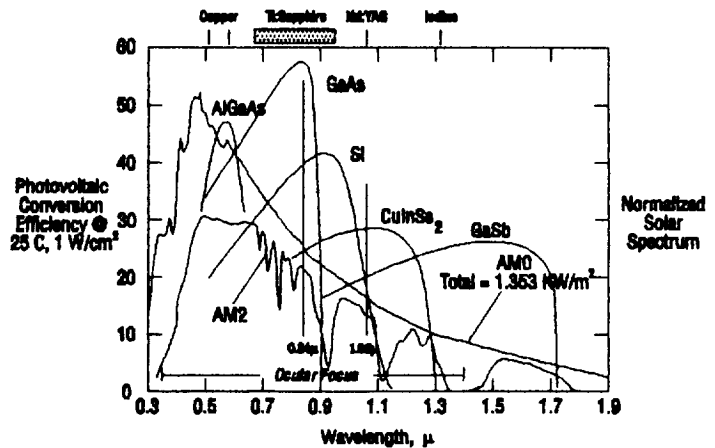

Fig. 2 Spectral Distribution

2

into that region as well. Technical difficulties with the laser and optics become dramatically worse at shorter wavelengths, so AlGaAs offers no advantages, and the low efficiencies of the IR cells would offset their other benefits (although ocular damage could ultimately prove to be an overriding consideration if beaming were to take place below the Earth's limb.)

Low power semiconductor and Ti:sapphire solid-state lasers are the only conventional devices to meet this unique wavelength requirement today, but the free electron laser (FEL) at least in concept offers virtually unlimited wavelength flexibility together with the potential of reliable, extremely high power operation without the massive flows associated with fluid mediums or the optical degradation of solid ones. Because of its demonstrated high power capability (over 1 GW at microwave frequencies) and the potential reliability of its all-solid-state and highly-modular architecture, the induction linear accelerator FEL was the system of choice during much of the SELENE program. The induction linac uses independent cavities which each accelerate the electron beam through a fixed voltage via magnetic induction and, being a low impedance machine, can accelerate very high currents in pulses with lengths on the order of tens of nanoseconds at several kilohertz repetition rates. However, these characteristics that made the induction linac so attractive in the past as the beam source for a weapon have proved to be its undoing for laser power beaming to photovoltaic receivers, and interest has turned to the use of other types of accelerators, specifically the RF linac and the Microtron. The RF accelerator, which unlike the induction has already been operated at short wavelengths, uses a microwave field with a highly-relativistic phase velocity to accelerate the electrons, and, though limited to much lower peak currents, produces closely-spaced micropulses with lengths of tens of picoseconds, thereby producing quasi-CW interactions. From the operational standpoint, they and their klystron power supplies are proving to be very reliable, and years of valuable experience have been gained with them at SLAC as well as at other facilities around the world. Another very promising concept, the Microtron in which the electron beam travels in a tightly-spiraled path in a fixed magnetic field and is recirculated through a set of RF cavities, has been extensively pursued by investigators in the former Soviet Union, and collaboration on it is now underway in the US.

The free electron laser is the only single means of producing coherent radiation over frequencies extending from the microwave into the soft X-ray, and is therefore likely to continue to receive attention from at least the university sector. However, the types of applications of interest to the researchers, together with the cost of components and facilities for high power operation, will limit the scope of those efforts, and the R&D that will be needed for the class of FELs that would be suitable for power beaming, waste treatment, bulk sterilization, and the like will cease if funding from DoD and NASA is curtailed. The excesses of the past have arisen from weak management and cost controls, not from fundamental and unavoidable technical difficulties, and a well-run unified program needs to be defined and undertaken so that the nation can finally benefit from this very promising technology.

The problems with pulsed operation of a photo-voltaic array can be seen in Fig. 3 which essentially gives the variation of conversion efficiency with total series resistance (load plus internal) and short-circuit current, the latter being proportional to a suitably averaged illumination level. While the maximum efficiency shows a fairly substantial logarithmic increase as the intensity rises, excursions of more than about a factor of two from optimum resistance can dramatically degrade performance. To put matters in perspective, one solar unit corresponds to about $I_{sc}/I_0 = 2 \cdot 10^4$ with silicon, while the power beaming program is interested in pulsed irradiation with time-averaged levels of at least a few suns and with peak levels about 1000 times the average. The optimum load varies approximately inversely with the illumination level, and very high intensities can eventually cause the internal cell
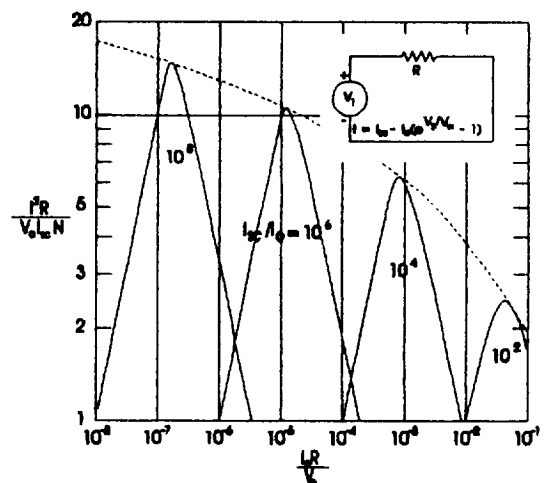

Fig.3 Photovoltaic Response

resistance alone to exceed the optimum value. Landis suggested two years ago that high currents resulting from strong irradiation could produce unacceptable losses in the internal series resistance, but that the minority carrier lifetime of the cells (a measure of the time for recombination after light-induced charge separation) could act to smear shorter pulses, effectively integrating them over that scale and reducing the peak currents. The result would be such that the large values for indirect bandgap materials like silicon would integrate the pulses in both cases, causing the cells to respond to the average intensity, whereas the shorter lifetime for direct bandgap materials like GaAs (comparable to the induction pulses) would smear only the short pulses (Fig. 4) and cause the cells to respond to the peak intensity of the longer ones with high currents and large series-resistance losses. This was confirmed by measurements in Feb 92 at LLNL and Rocketdyne by NASA personnel using conventional lasers with simulated induction and RF formats: the results showed that silicon operated nicely with either, but that both conventional and concentrator GaAs cells gave far better performance with the shorter pulses.
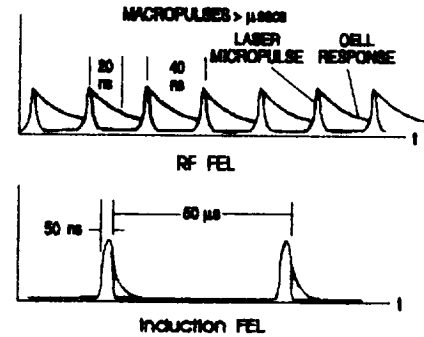

Fig. 4 GaAs Photovoltaic Response to FEL Irradiation

Various means for alleviating the problem for the induction FEL were studied by this author, including both capacitive loading and series connection to reduce the resistance, and pulse lengthening via splitting and delay to reduce the peak currents, but none proved to be particularly cost-effective, and efforts were terminated when it was realized that the problem lay not just in the pulse duration but in the interpulse time as well. The fact is that the required accuracy and dynamic range may be quite difficult and costly to achieve if the system is to be truly multi-purpose by being be able to accommodate both solar irradiation and the large peak currents from laser pulses. Fortunately, the minority carrier lifetimes of both GaAs and silicon are such that the pulse train from an RF FEL (at least within a macropulse) will be effectively averaged into a CW-like output from the cells -- but the interpulse times for the induction FEL are long even compared to the silicon lifetime so the cell output will remain pulsed with that laser.

The problem with any laser beam is further complicated by the nearly-gaussian distribution of intensity about its centroid at the focus and by the centroid wander produced by both system jitter and atmospheric turbulence. Unless the receiver were flood-loaded with a much larger beam, the spatially and temporally varying illumination would require active load compensation for fully optimum operation, and that would considerably complicate the array design. The effects of various loading schemes have been analyzed by considering independent receiver elements each with its own load resistance, a model which should give a reasonable representation of the behavior of parallel-connected cells (see Attachment G for an analysis of photovoltaic operation with laser illumination.) The maximum total power output with identical elemental circuits and gaussian illumination is achieved if the load is optimized for about 55% of the peak short circuit current, and Fig. 5 compares the distributions of output power density and included power for optimum fixed resistance with those for locally-optimized ("active") loading for a typical case with $I_{sc}/I_o = 10^6$. The value of the fixed resistance is higher than optimum in the high-intensity central region and lower in the wings, so the efficiency is somewhat less than would be achieved with the locally-optimized loading (24% less for the sample case.) The rather nominal performance penalty may prove to be a very small price to pay, however, when one considers that the locally-optimized loading would have to be "active" at relatively high frequencies to account for centroid motion, whereas, although the constant-resistance "passive" load might
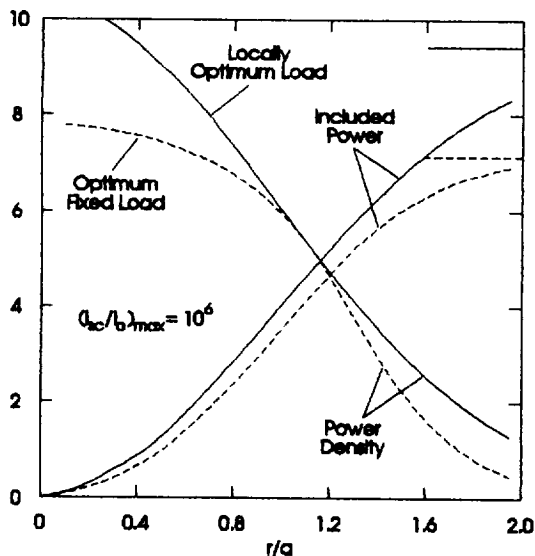
Fig. 5 Distribution of Optimized Response to Gaussian Irradiation

have to be variable as well to account for changes of peak intensity (particularly for space vehicles), its variations would be applied on a global scale at much lower frequencies. Furthermore, while 86.5% of the incident power is included within the $1/e^2$ radius r = 2a, that same fraction of the output power for the case of Fig. 5 is included within r/a = 1.89 with local optimization and only 1.55 with the optimum constant load, thereby providing the possibility of a smaller receiver.

Photovoltaic cells are intended for relatively uniform flux and are not well-suited to pulsed laser irradiation, but their performance is understood and they are well-developed for space operation. The temptation to seek alternative conversion schemes should be overcome, and means should be sought to best adapt them to laser irradiation, but it must be established early on that this can in fact be done without compromising overall system performance.

A second serious consequence of the pulse format of the induction FEL is the fact that the physical length of a pulse is on the order of ten meters while the pulse spacing is tens of kilometers. Unless an extremely long path is used as a delay line to interfere successive pulses, the induction FEL cannot therefore be used as a resonator, and a relatively powerful master oscillator must be used at the appropriate wavelength. The problem was considered difficult but at least solvable with operation at 1.06 microns with the highly-developed Nd:YAG or Nd:glass lasers (LLNL wanted 30M$ to develop one even after all the experience that had been gained with the SHIVA and NOVA ICF systems), but, as noted earlier, only semiconductor and Ti:sapphire lasers operate in the 0.8 - 0.85 micron region required by the photovoltaic receivers, and those systems have been demonstrated only at very low power levels. RF FEL micropulses, on the other hand are much shorter (generally less than a centimeter), and the spacing between them is only a few meters, so they can easily be operated as resonators without a separate driver.

Progress with semiconductor and solid state lasers should be monitored for their application to power beaming, not just as drivers for FEL amplifiers, but rather for use as the primary laser. Rapid advances being made in diode pumping promise major improvements in both efficiency and beam quality, and, if the elusive means can be found to lock multiple cavities together in phase, a myriad of coupled lasers could prove most attractive. That would especially be so if the entire system could function as a phased array with the locking signal coming from the receiver, thereby automatically compensating for disturbances along the path.

Turning now to propagation, a coherent monochromatic beam of wavelength λ from an aperture with diameter D is spread with a half-angle of about λ/D by diffraction. The resulting ideal peak intensity and spot size are shown in Fig. 6 at 0.84 μ with a gaussian beam truncated at $1/e^2$ (the latter is near-optimum shaping for an FEL, but the effect is a minor one here.) Beaming to a realistic receiver beyond a very low orbit will clearly require a large aperture, and the 12 mW/sq.cm./MW telescope being considered for SELENE will produce a 5 m spot in GEO and a 50 m one on the lunar surface (for comparison, the deployable solar panels on the Hubble Space Telescope are each about 12 m long.) Errors in the source beam and index variations along the optical path will cause instantaneous energy spread beyond the ideal size, and mechanical jitter will cause further time-averaged spread (λ/D is only 70 nrad with a 12 m telescope at 0.84 μ), and some of the energy may prove to be impossible to recover. Whereas phase aberrations over scales comparable to D will affect the distribution of the central
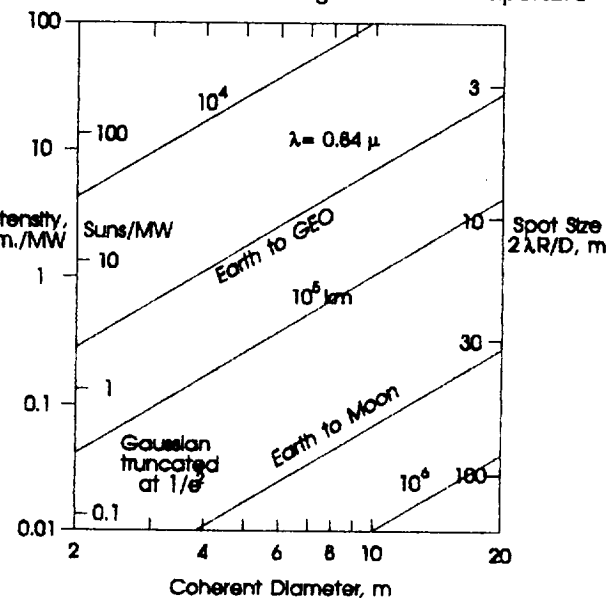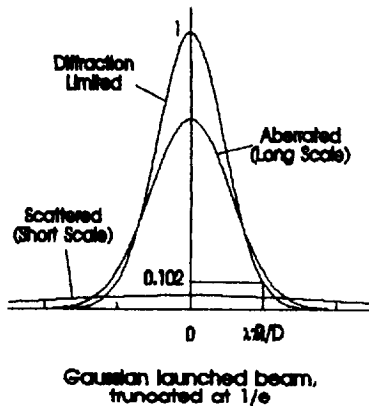

Fig. 6 Beam Propagation

5

Fig. 7 Real Beam Profile

lobe itself, small-scale disturbances with an RMS phase error ϕ and lateral correlation scale d << D will scatter a factor of about $1-\exp(-\phi^2)$ of the power into a much broader beam of half-angle λ/d, effectively producing a composite profile (Fig. 7) with an attenuated but otherwise undisturbed central lobe surrounded by very low-level and widely-spread energy. Thus, 9.1% of the power is scattered for $\lambda/20$ RMS wave distortion, and this rises rapidly to 33% at $\lambda/10$, so it is imperative that errors be small. The same is true whether the system is for power beaming or imaging, but there is an important distinction between them in that, for the same degree of degradation, the central lobe may be sufficiently strong to provide the required resolution and signal strength for imaging, whereas it may be totally inefficient for beaming (this can prove to be particularly important in weighing the significance of data from adaptive optics tests.) In either case, the scattered energy is effectively lost. Since FELs tend to produce "perfect" beams (aside from correctable errors introduced in the external optics), the central core should be very close to the ideal size -- although certainly attenuated -- and additional allowance need only be made for centroid motion from mechanical jitter and uncorrected atmospheric tilt. It should be noted that thermal blooming, a major source of central core distortion with many other high power laser systems, does not appear to be a problem here (at least in the expanded beam) primarily because of the low absorption at 0.84 μ and the large apertures being used, and the adaptive optics system should be able to accommodate minor contributions from it as long as care is taken to ensure that there is always sufficient crosswind to sweep away the heated air. Nevertheless, it has been a major problem in the past, and should be reconsidered if changes are made in any of the key design parameters.

The scattered portion of the beam arises primarily from the density variations produced by atmospheric turbulence, and the adaptive optics system required to compensate for them is the second key area, besides the free electron laser, for which extensive R&D is still required. This entails several intimately-related elements:

- a synthetic beacon, target return, or other source that provides a reference signal,
- sensors that measure the source signal and optical component motion,
- algorithms that translate the data into commands,
- actuators that drive the components, and
- the phase correction elements themselves.

The effects of turbulence on a beam inclined at an angle Θ from zenith are characterized by the Fried coherence length

$$r_o = 0.185 \, (\lambda^2 \cos\Theta \, / \int C_n^2(h) \, dh)^{3/5}$$

for a uniform plane wave and a Kolmogoroff spectrum, and it has been demonstrated that appreciable improvement can be realized in both imaging and beaming applications if the disturbed wavefront is properly corrected over dimensions of r_o or less. A representative spatial distribution of turbulence strength, the Hufnagel-Valley profile is shown in Fig. 8, and displays the high level of turbulence normally found very near the ground, the "spike" associated with the tropospheric wind shear layer, and the otherwise pronounced decay with altitude; not shown is the highly-stratified behavior that arises from velocity shear and local disturbances, but
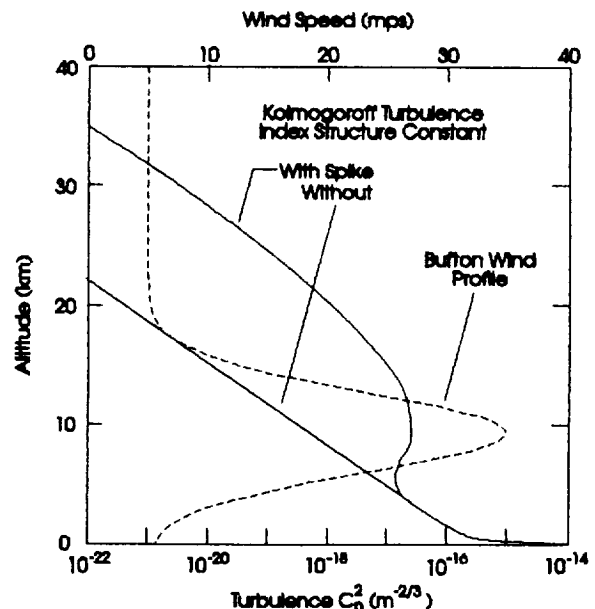

Fig. 8 Turbulence and Wind Profiles

6

those variations are smoothed by the path integration for ground-to-space propagation. With the H-V profile, 73% of the contribution to r_0 arises from the ground layer alone and only 9% is due to the "spike".

There has been a tendency to concentrate on the path through the free atmosphere, but an area that should, perhaps, be of greater concern is the turbulence produced by the beam director itself and by thermal blooming in the high-intensity optical path within it. The severe turbulence near the ground is due to the earth's boundary layer, obstructions in the wind, and thermal gradients, so, since the power beam is directed upwards (rarely exceeding 65 degrees from zenith), it may be possible to design the telescope enclosure and the immediate surroundings to mitigate the generation of strong turbulence, thereby substantially increasing the turbulent coherence scale r_0. Similarly, the fundamental cause of thermal blooming is absorption by molecules and aerosols in the optical path, and a means must be found for maintaining an acceptable environment within the telescope. Neither of these need involve massive computational efforts, but they must be done, and they'll require careful design engineering with attention paid to the basic mechanisms.
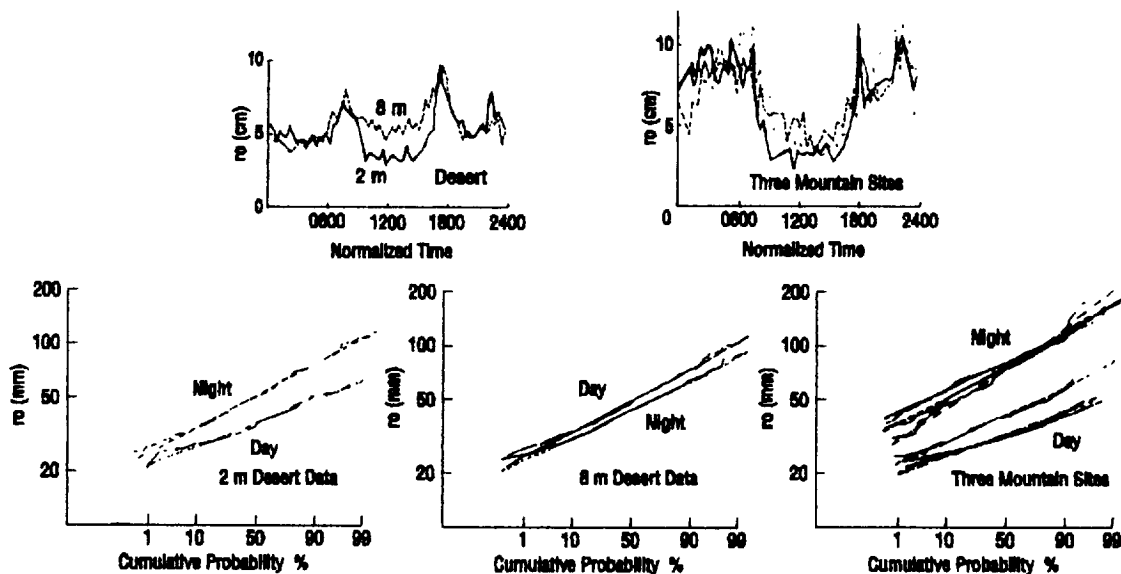

Fig. 9 WSMR Star Trail Data

Fig. 9 shows the results of a comprehensive series of star trail measurements taken at WSMR. These are unusual in that they have been presented -- as all turbulence data should be -- in terms of probability of occurrence, and this is especially important for laser power beaming to space because the worst-case situations of large angles from zenith and high-slew rates for which compensation is most difficult are also likely to be relatively rare and unduly stressing and should not be used alone to define the system requirements (e.g., r_0 at Θ = 75° is 2.25 times smaller than that at small angles.) The data suggests that r_0 in all cases is greater than 30 mm 90% of the time; this translates to 5 cm when scaled from the mid-visible (0.55 µ) to 0.84 µ (the H-V model predicts 9 cm at the longer wavelength.)

The design value of 3 cm dictated for use as the segment size in the SELENE program is an admirable goal, and should be sought if it can be done, but it is smaller than necessary for good overall system performance, and the penalties for using such a small size (e.g., 160,000 elements with a 12 m telescope) should be carefully weighed.

A complete methodology for estimating the actuator requirements for adaptive optics correction of global tilt and residual piston error arising from Kolmogoroff atmospheric turbulence is presented in Attachment E. The primary advantage of global tilt removal is that large control displacements are required only at relatively low frequencies, whereas, if not done, the high-frequency controls for the

7

individual segments would have to be capable of considerably larger strokes; the cost/benefits of a separate global tilt correction system would depend upon the particular implementation and should separately be addressed. Assuming an $r_0 = 4$ cm with segments of the same size in view of the afore-mentioned arguments, the analysis predicts RMS requirements for global tilt, piston, and subaperture tilt correction of 3.30 μrad, 42.4 rad, and 8.53 μrad respectively for a 12 m aperture. Using a 2.5X multiplier as justified in the attachment, these would translate into peak-to-peak values of 4.1 μ for edge stroke of a 1 m global tilt corrector (12X magnification), 13.5 μ for piston, and 0.05 μ for additional edge stroke of the piston to correct for subaperture tilt. The required frequency response of the actuators is equally important, and that depends upon the speed at which the turbulence is swept across the beam; that issue is addressed as well in the same attachment, and generalized results are given for a uniform crosswind, a Bufton-like profile (Fig. 8), and slew-induced "wind." Subject to representative conditions described there, and considering two particular cases of interest, one with beaming only to high orbits where the velocity would be given by the Bufton profile and the other for beaming to a 300 km orbit for which slew would be the dominant wind source, the cutoff frequencies for global tilt correction would be 2.9 HZ and 39 HZ respectively, while those for residual piston correction would be 130 HZ for the high-orbit system and 1350 HZ for the low.

Low-orbit applications clearly impose extremely severe requirements on the AO system (and, of course, on the slew mechanism), so a shared system with a much smaller dedicated beam director -- which would be effective at short ranges -- might prove optimum for beaming to LEO with far fewer high-frequency elements. For example, a 2.2 meter telescope operating at 0.84 μ will produce a 2.3 m spot at 3000 km range, and this will require only 3025 4 cm elements as compared to the 90000 elements in a 12 m system -- all of which would have to respond at high frequency! Although the global tilt control of the smaller system would have to respond to about 180 HZ, the required throws of all of the actuators would be about 4X smaller, and the larger system could be designed for the less-stressing high-orbit applications alone.

An adaptive optics system corrects for phase errors by adjusting the optical path length by an amount equal and opposite to that caused by the disturbances; nothing is done to correct for the less important (but non-negligible) degradation caused by intensity fluctuations. The most accurate approach for phase control is via direct measure of the end-to-end optical path length variation across the beam with individual interferometry at each segment to define the piston displacements required for correction (at least within an ambiguity of 2π), but this is probably the most difficult and costly to implement by far. A Hartmann sensor to measure the local slope of the wavefront at each segment is less complicated and has become the technique of choice for adaptive optics, but that advantage is balanced by the needs to convert the slope information to wavefront shape via Poisson's equation and to establish a reference (or references) from which to measure the shifts. The latter would be trivial with a conventional optical bench, but a large power beaming telescope structure is unlikely to provide such an accurate base, and additional measurements will be needed to relate either the heights or references of adjacent segments (for example, the lightweight millimeter-wave truss design being considered for SELENE is "precise" only at microwave scales and is quite flexible at optical ones.)

Although the adaptive optics system should in theory be able to compensate for deflections of the telescope structure as well as for the disturbances from the atmosphere, most of the Poisson solutions involve some type of edge matching as the basis for commanding the actuators, and it is quite doubtful that any of the proposed edge measurement techniques will be sufficiently accurate to prevent an unacceptable error buildup across the beam if used throughout to give a "relative reference." Displacements everywhere must be controlled to within at least $\lambda/20$ as noted earlier, and probability requires that relative displacements over a linear path involving N measurements from an arbitrary reference then each be accurate to a factor of at least $1/\sqrt{N}$ of that; N would be about $\sqrt{(90000/\pi)} = 169$ for a system with 90000 segments and $\lambda = 0.84$ μ, and that could therefore require a measurement accuracy of about 30 angstroms! On the other hand, a very promising alternative appears to be the deterministic solution scheme proposed last year by AMP *which gives the required piston and tilt displacements of each segment directly without iteration and without involving the error buildup of other techniques,* but it does rely for its success upon the ability to establish an accurate reference surface

from which the piston displacements can be measured (Attachment F describes the application of the approach to hexagonal segments.) Although the predicted edge differences can in theory be used to individually adjust the segments (or each be combined with the local average tilt to give the piston differential across the gap), the differences are likely to be so small that measurement errors will accumulate excessively, and they should be used instead in groups to specify piston displacements from a common reference piston -- *not each with reference to a nearest neighbor.* There appears to be no obvious way of providing a single absolute reference over the scale of the entire aperture, but a workable compromise should be afforded with a hybrid system using the AMP technique to provide local control of a large number of small segments grouped on rigid "super segments" that would in turn be either interferometric or edge referenced to connect them and externally controlled only to compensate for the large-scale low-frequency flexing of the telescope structure and perhaps global tilt from turbulence. In view of the limited number and low actuation frequency of the large segments, it might be useful to reassess the closed-loop multi-dither control approach from the early 70's, using target return and iteration to maximize intensity.

Program Recommendations

Work on power beaming, at least in the near future, will have to be carefully prioritized in view of the amount that needs to be done and the limited funds available to support it.

The FEL is one of the major elements of the system and considerable development will be needed to achieve short-wavelength operation at the conditions of interest, but that work, and especially the hardware needed to accomplish it, could prove to be expensive. It appears now that the pulse format of the induction FEL is incompatible with efficient photovoltaic power conversion and that the CW-like operation of the RF FEL will yield superior performance, but the latter may not as easily admit modular growth, and a new development plan with key milestones will have to be formulated. A program is in place for a 100kW 10μ RF FEL at Boeing and Los Alamos, Rocketdyne has most of the components for a 1kW 1μ system, research efforts are underway at Duke (with Russian support), Vanderbilt, and other laboratories, and there remains a wealth of induction FEL experience at LLNL, SRL, MIT and elsewhere. A working group with knowledgeable participants from that community and from the government should assess the status of the RF FEL and develop realistic costs and schedules for a program leading to a 10 MW 0.84μ system. In addition, the potential cost and reliability advantages which made the induction FEL attractive in the past of course remain, and efforts should continue to be made to adapt that system to power beaming.

The area that must receive the greatest attention in the near future is the adaptive optics, and the PAMELA hardware being acquired by MSFC for use there should provide an excellent test bed for sensors, algorithms, and actuators. An important test of the concepts should be to mount that or similar equipment on a full-size truss telescope structure to demonstrate that compensation can indeed be accomplished on a system level, and the key technical results of that work should be the specification of component requirements and the levels of control ("woofer/midrange/tweeter") required for the most cost-effective operation. A working group with participants from at least MSFC, JPL, FORTH, KAMAN, AMP, and MITLL should periodically review that effort. An important area that has been largely neglected to date in this program is the synthetic beacon (or beacons) that will be required to provide the reference signal for the adaptive optics, and MITLL should be contracted to establish those requirements.

The potentially high performance of the SRL/TRW electrodeless thruster could be extremely important for space transportation and work on it needs to be funded, but another source should be found to do so in view of its applicability to a broad range of NASA interests beyond power beaming

Finally, high-level application studies should be conducted specifically to attract advocates from both the government and commercial communities, and an effort should especially be made to obtain the backing and resources of major aerospace and telecommunications contractors to whom power beaming could offer considerable long range benefits.

9

Attachments

The attached technical reports were completed during or after the contractural period:

A.	Optimum Segment Fitting to a Parabolic Surface	– 5 / 92
B.	Optimum Segment Fitting to a Parabolic Surface - Part II	– 5 / 92
C.	Optimum Gaussian Truncation	– 5 / 92
D.	EOTV Orbital Transfer	– 7 / 92
E.	Actuator Requirements for Turbulence Compensation	– 2 / 93
F.	Deterministic Control of Hexagonal Segmented Mirrors	– 3 / 93
G.	Some Aspects of Photovoltaic Power Conversion with Laser Illumination	– 3 / 93

Distribution

NASA Headquarters:	Dr. John D. G. Rather, NASA HQ Code C, 300 E St, Washington DC
NASA MSFC:	Mr. Edward E. Mongomery IV, PS04, NASA MSFC AL 35812
	Mr. James W. Bilbro, EB23
	Mr. Whitt Brantley, PD01
NASA Lewis:	Mr. John Bozek, MS 301-5, 21000 Brookpark Rd., Cleveland OH 44135
	Dr. Geoffrey Landis, MS 302-1
Jet Propulsion Lab.:	Dr. George E. Sevaston, T1710, 4800 Oak Grove Dr., Pasadena CA 91109
	Dr. Bruce Anspaugh, MS 183-167
	Dr. David Redding
Naval Weapons Center:	Dr. Hal Bennett, NAWC WPNS, Code 38101, China Lake CA 93555
Naval Postgrad School:	Dr. David L. Fried, Monterey CA 93943
	Dr. William B. Colson
AMP Research:	Dr. Shirley Enguehard, PO Box 383, Lexington MA 02173
Boeing Co.:	Mr. Gordon Woodcock, PO Box 240002, Huntsville AL 35824
COMSAT:	Dr. Andrew Muelenberg, 23000 Comsat Dr., Clarksburg MD 20734
Duke Univ. FEL Lab.:	Dr. John Madey, LaSalle Street Ext., Durham NC 27708-0319
	Dr. Vladimir Litvinenko
	Dr. David Straub
Forth Inc.:	Dr. Edward K. Conklin, 111 N. Sepulveda Blvd., Manhatten Beach CA 90266-6847
Kaman Sciences Co.:	Dr. Albert J. Lazzarini, PO Box 7463, Colorado Springs CO 80933-7463
	Dr. Gregory Ames
Lawrence Livermore:	Dr. Irving Stowers, L-791, PO Box 808, Livermore CA 94550
	Dr. Ted Scharleman, L-465
	Dr. Herb Friedman, L-464
MIT Lincoln Laboratory:	Dr. Darryl P. Greenwood, 244 Wood St., Lexington MA 02173
MIT Plasma Fusion Ctr.:	Dr. Bruce Danly, MIT NW16-172, Cambridge MA 02139
Quantametrics:	Dr. John Remo, #1 Brackenwood Path, St. James NY 11786
Rocketdyne:	Dr. Robert J. Burke, FA60, 6633 Canoga Ave., Canoga Park CA 91308
Science Research Lab.:	Dr. Jonah Jacobs, 15 Ward St., Somerville MA 02143
	Dr. Daniel Birx, 3300 Crismore, Oakley CA 94561
	Dr. Joseph Mangano, 1530 N. Key Blvd., STE 1816, Arlington VA 22709
W.J. Schafer Associates:	Dr. Donald Ponikvar, STE 800, 1901 Ft. Myer Dr., Arlington VA 22209

# OPTIMUM SEGMENT FITTING TO A PARABOLIC SURFACE

Dr. Glenn W. Zeiders, The Sirius Group

Calculations have shown that small segments with a fixed spherical figure can be used to approximate the surface of a parabolic mirror with satisfactory accuracy if the F/number is sufficiently large, and that there is very little benefit to using multiple spherical curvatures because most of the error is due to local astigmatism (different radial and azimuthal curvatures) of the parabola. However, advances in deterministic mirror figuring, such as LLNL's precision diamond machining, Itek's computer-controlled optical surfacing (CCOS), and Kodak's ion sputtering, may permit cost-effective, large-volume manufacturing of aspheric segments, and this paper explores the use of a limited number of different aspheric segments, carefully arranged to make best use of the basic hexagonal segment shape. The results indicate a significant benefit if the aspheric surfaces can be economically mass-produced .

ANALYSIS

A paraboloid is described by

$$z = \beta r^2 = r^2 / 4F \; , \; dz/dr = 2\beta r = \tan \varphi,$$
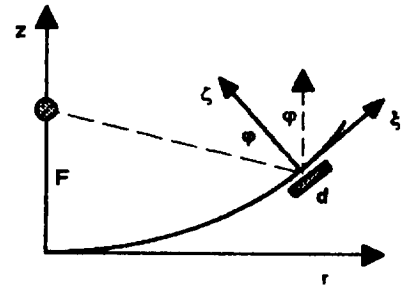
and the segment surface coordinates (ξ, η, ζ) are related to fixed-space coordinates (x, y, z) for a segment defined to be located on the x-axis by

$$x = r + \xi \cos \varphi - \zeta \sin \varphi \, , \; y = \eta \, , \; z = \beta r^2 + \xi \sin \varphi + \zeta \cos \varphi,$$

from which it follows that
$$\zeta = \beta (\xi^2 \cos^2 \varphi + \eta^2) \cos \varphi = \beta (\xi^2 + \eta^2 \gamma^2) / \gamma^3,$$

neglecting terms of order d/F relative to unity and where

$$\gamma^2 = \sec^2 \varphi = 1 + (2 \beta r)^2.$$

It can be seen from inspection of these equations that the local radial and azimuthal radii of curvature are given by $2 \beta R_r = \gamma^3$ and $2 \beta R_\theta = \gamma$.

Now, letting the segment surface figure be astigmatic with radii R_x and R_y defined in cartesian space, the mean square distortion across a circular segment of diameter d (d = 1.0501 x the face-to-face width of a hexagon of the same area) is given by

$$\delta^2 = (4/\pi d^2) \int_0^{d/2} \oint [\delta_0 + \rho^2 \{\cos^2(\theta + \varphi)/2R_x + \sin^2(\theta + \varphi)/2R_y - \beta \cos^2\varphi/\gamma^3 - \beta \sin^2\varphi/\gamma\}]^2 \, \rho \, d\theta \, d\rho$$

$$= \delta_0^2 + \delta_0 d^2 \{1/2R_x + 1/2R_y - (\gamma^2 + 1)/\gamma^3\}/8 + d^4 [(1/2R_x - \beta/\gamma^3)^2 + (1/2R_x - \beta/\gamma^3)(1/2R_y -$$

$$1/2R_x) - (1/2R_x - \beta/\gamma^3) \beta (\gamma^2 - 1)/\gamma^3 + 3(1/2R_y - 1/2R_x)^2/8 + 3\beta^2 (\gamma^2 - 1)^2/8\gamma^6 -$$

$$(1/2R_y - 1/2R_x) \beta (3 - 2\sin^2\theta)(\gamma^2 - 1)/4\gamma^3.$$

δ_0 is a simple "piston" correction that can be locally applied, and the optimum value is

$$\delta_0 = -d^2 \{1/2R_x + 1/2R_y - \beta (\gamma^2 + 1)/\gamma^3\}/16,$$

so that
$$\delta^2 = (d^4/192)[(1/2R_x - \beta/\gamma^3)(1/2R_y - \beta/\gamma) + 3\{1/2R_y - 1/2R_x - \beta(\gamma^2 - 1)/\gamma^3\}^2/4$$

$$+ 2\beta (1/2R_y - 1/2R_x)\sin^2\theta (\gamma^2 - 1)/\gamma^3.$$

For the special case of spherical segments, the two radii are equal, and the equation reduces to

$$\delta^2 = d^4 [\{1/R - \beta (\gamma^2 + 1)/\gamma^3\}^2 + 2\beta^2 (\gamma^2 - 1)^2/\gamma^6]/768.$$

Note that optimal variation of the spherical radius of curvature, i.e. $\beta R = \gamma^3/(\gamma^2 + 1)$, would still result in an appreciable astigmatic contribution from the second term. Averaging over a region from $D_1/2 = \alpha D/2$ to $D/2$, the overall mean square variation of the *output wavefront* is therefore given by

$$<\delta_w^2> = [4/\{\pi D^2 (1 - \alpha^2)\}] \int_0^{d/2} \delta^2 \, 4 \sec^2\varphi \, 2\pi \, r \, dr = (8/\beta^2 D^2) \int_{D_1}^{D} \delta^2 \gamma^3 \, d\gamma$$

$$= (d^4/96 D^2)[(\gamma^2 - 1)/(4\beta^2 R^2) - 2\{(\gamma^3 - 1)/3 + \gamma - 1\}/(\beta R) + (\gamma^2 - 1)/2 + 2\ln(\gamma) +$$

$$(\gamma^2 - 1)/(2\gamma^2) + 2\{(\gamma^2 - 1)/2 - 2\ln(\gamma) + (\gamma^2 - 1)/(2\gamma^2)\}].$$

from which it follows that the optimum *constant spherical* radius of curvature is given by

$$(\gamma^4 - \gamma_1^4)/(4\beta R) = (\gamma^3 - \gamma_1^3)/3 + \gamma - \gamma_1,$$

so that
$$<\delta_w^2> = (\beta^2 d^4/96)[3\{1 + 1/(\gamma^2\gamma_1^2)\}/2 - 2\ln(\gamma)/(\gamma^2 - \gamma_1^2) -$$

$$4(\gamma^2 + \gamma\gamma_1 + \gamma_1^2 + 3)^2/\{9(\gamma^2 + \gamma_1^2)(\gamma + \gamma_1)^2\}]$$

$$= (\beta^2 d^4/192)[(1 + \alpha^4)\varepsilon^4 - (19 + 4\alpha^2 + 7\alpha^4 + 18\alpha^6)\varepsilon^6/12 + \dots]$$

where $\varepsilon = \beta D = D / 4F$. The segment size requirements for a full aperture ($\alpha = 0$) are shown in Fig. 1 for both a continuously variable optimum spherical figure and a constant optimum spherical curvature. The two differ by only about 10% because of the dominance of the astigmatic term, so it would not be cost-effective to vary the spherical curvature either continuously or piecewise across the aperture.

Returning to the case of an astigmatic correction and integrating that expression over the annular region, we obtain

$$< \delta_w^2 > \; = \; [d^4 / \{48 \, D^2 \, (1 - \alpha^2)\}] \, [(\gamma^4 - \gamma_1^4) / (8 \, \beta^2 \, R_x \, R_y) - (\gamma^3 - \gamma_1^3) / (3 \, \beta \, R_x) - (\gamma - \gamma_1) / (\beta \, R_y) +$$

$$3 \, (\gamma^4 - \gamma_1^4) \, \{1 / (2 \, \beta \, R_y) - 1 / (2 \, \beta \, R_x)\}^2 / 8 + 3 \, (\gamma^2 - \gamma_1^2) \, \{1 + 1 / (\gamma^2 \gamma_1^2)\} / 4 - \ln(\gamma / \gamma_1) -$$

$$\{(\gamma^3 - \gamma_1^3) / 3 - \gamma + \gamma_1\} \, \{1 / (2 \, \beta \, R_y) - 1 / (2 \, \beta \, R_x)\} \, \{1 + 2 \, (\sin \theta) / \theta\}],$$

from which the optimum curvatures are found to be given by

$$(\gamma^4 - \gamma_1^4) / (4 \, \beta \, R_y) \; = \; (\gamma^3 - \gamma_1^3) / 3 + \gamma - \gamma_1 + \{(\gamma^3 - \gamma_1^3) / 3 - \gamma + \gamma_1\} \, (\sin \theta) / \theta$$

and

$$(\gamma^4 - \gamma_1^4) / (4 \, \beta \, R_x) \; = \; (\gamma^3 - \gamma_1^3) / 3 + \gamma - \gamma_1 - \{(\gamma^3 - \gamma_1^3) / 3 - \gamma + \gamma_1\} \, (\sin \theta) / \theta.$$

Thus,

$$< \delta_w^2 > \; = \; (\beta^2 \, d^4 / 96) \, [3 \, \{1 + 1 / (\gamma^2 \gamma_1^2)\} / 2 - 2 \ln(\gamma) / (\gamma^2 - \gamma_1^2) -$$

$$4 \, (\gamma^2 + \gamma \gamma_1 + \gamma_1^2 + 3)^2 / \{9 \, (\gamma^2 + \gamma_1^2)(\gamma + \gamma_1)^2\}] -$$

$$8 \, (\gamma^2 + \gamma \gamma_1 + \gamma_1^2 - 3)^2 \, \{(\sin \theta) / \theta\}^2 / \{9 \, (\gamma^2 + \gamma_1^2)(\gamma + \gamma_1)^2\}]$$

$$= \; (\beta^2 \, d^4 / 192) \, [(1 + \alpha^4) \, \varepsilon^4 \; - \; (19 + 4 \, \alpha^2 + 7 \, \alpha^4 + 18 \, \alpha^6) \, \varepsilon^6 / 12 + \ldots$$

$$- (1 + \alpha^2) \, \{(1 + \alpha^2) \, \varepsilon^4 / 2 \; - \; [(1 - \alpha^2)^2 / 6 + (1 + \alpha^2)^2] \, \varepsilon^6 / 2 + \ldots\}\{(\sin \theta) / \theta\}^2]$$

This is plotted in Fig. 2, again as segment size vs. f/number for 1/20 wave distortion @ 0.8 μ with a 12 m aperture, and the results are shown for astigmatic segments with $30°$ and $60°$ included angles and for annuli with $\alpha = 0.5, 0.8,$ and 1; the equivalent results for segments with constant spherical figure over the annuli are shown for comparison. Unlike the all-spherical case where little is gained by segmentation, relatively coarse segmentation with astigmatic elements can offer significant benefit, but it should be noted that very fine annuli (i.e., $\alpha \to 1$) offer a benefit only with very fine angular segmentation as well ($\theta \to 0$), and that would not be likely to be cost-effective.

Key to mass-production of aspheric elements by any of the new deterministic surface figuring techniques is the amount of material to be removed after an initial spherical figure is applied. It follows that the maximum aspheric thickness to be removed with the optimum astigmatic segments is

$$d^2 \, (1 / R_y - 1 / R_x) / 8 = (d^2 / 12F) \, (\gamma^2 + \gamma \gamma_1 + \gamma_1^2 - 3) \, \{(\sin \theta) / \theta\} / \{(\gamma^2 + \gamma_1^2)(\gamma + \gamma_1)\}$$

$$= (\varepsilon^2 \, d^2 / 16F) \, (1 + \alpha^2) \, \{\sin \theta / \theta\} + \ldots$$

As an example, 0.54 μ would be the maximum aspheric thickness that would have to be removed from 4 cm segments for a 12 m, f/1 mirror having an astigmatic zone with θ = 60° and α = 0.5. While large compared to the 0.02 μ figuring tolerance at 0.8 μ wavelength, it's small compared to the $d^2/16F$ = 8.3 μ spherical well depth, and it should be possible to accurately remove the material in a single pass.

SYSTEM OPTIMIZATION AND RESULTS

A set of computer experiments were conducted to determine the "optimum" configurations for use with hexagonal mirror segments, noting that 60° sections are repeated, and that integer fractions of 60° simply require that the primary axes be rotated relative to an edge. Every possible combination for up to six different individual segment configurations were tried, and the results for the best solutions are given in Table I for an annular primarily mirror with an inner diameter of 10% of the outer and, except for the spherical reference case, for an inner astigmatic ring with identical segments (ie., repeated every 60°.) The results are again presented in terms of the required equivalent circular diameter for 0.04 μ RMS wavefront distortion over a 12 meter mirror (in bold type), and the inner diameters of the astigmatic zones are given in italic type. The geometries are shown in Fig. 3.

Number of Different Figures	Number of Different Segments	Angular Size of Outer Zones	F/Number				
			0.5	1.0	1.5	2.0	2.5
1	1	Spherical	**0.7979**	**2.1136**	**3.8317**	**5.8715**	**8.1875**
1	1	60	**0.8995**	**2.3608**	**4.2720**	**6.5417**	**9.1193**
2	2	60	*0.686*	*0.704*	*0.708*	*0.709*	*0.710*
			1.0625	**2.8077**	**5.0873**	**7.7939**	**10.8673**
2	3	30	*0.663*	*0.683*	*0.688*	*0.689*	*0.690*
			1.2204	**3.2036**	**5.7968**	**8.8765**	**12.3740**
3	4	60	*0.512*	*0.534*	*0.539*	*0.540*	*0.540*
		30	*0.732*	*0.752*	*0.757*	*0.758*	*0.759*
			1.2997	**3.4237**	**6.1996**	**9.4958**	**13.2388**
3	5	30	*0.532*	*0.554*	*0.558*	*0.560*	*0.560*
		30	*0.790*	*0.805*	*0.809*	*0.810*	*0.810*
			1.3769	**3.6271**	**6.5676**	**10.0594**	**14.0246**
3	6	30	*0.522*	*0.543*	*0.549*	*0.550*	*0.550*
		20	*0.773*	*0.790*	*0.794*	*0.795*	*0.795*
			1.4630	**3.8406**	**6.9495**	**10.6416**	**14.8345**

Table I   Optimum Configurations with Astigmatic Segments

At a given f/# -- and if other considerations should allow it -- the segment size could be increased by 81% by using 6 different astigmatic segments (but with only 3 different figures), thereby decreasing the total number of segments by a factor of 3.3. Alternatively, were a system originally to be configured at f/1.5 on the basis of spherical segments, a similar design change would permit the use of a f/1.0 system, thereby decreasing the height of the secondary mirror structure by 33%. Furthermore, the inner zone probably doesn't require aspherics, because it has been found that the use of spherical segments there would only increase the minimum allowable segment size by a few per cent at most.

Note that results have been presented for a particular set of design conditions (0.04 μ RMS wavefront distortion over a 12 meter mirror), but the maximum allowable equivalent diameter can be scaled to other conditions by the fact that it is proportional to $(\delta_W D)^{1/2}$ for all other design parameters remaining unchanged. The dependence upon allowable distortion can be especially important because the useful power on target scales as $\exp[-(2\pi\delta/\lambda)^2]$ when the wavefront error correlation lengths for the disturbances are small (as they are here). Thus, the factor in the exponential loss scales as d^4 for this geometrical effect, whereas it scales only as $d^{5/3}$ for Kolmogorov turbulence, so it produces a much more dramatic loss than does atmospheric turbulence as the segment diameter increases beyond a certain value -- and that value may be increased significantly by the use of aspherics.

Although quite attractive from the performance standpoint, the ultimate cost effectiveness of aspherics will depend upon the ability to produce them economically in large quantities.

The formula manipulations in this paper are straightforward but painfully lengthy, and details have been presented only to indicate the approach or to give important results. Details are available from the author upon request.

$\delta_w = 0.04\mu$ (1/20 wave @ 0.8 μ, S.R. = 0.906)
$D = 12m$
$d \propto (\delta_w D)^{1/2}$

Continuously Variable
Optimum Radius of
Curvature

Constant Optimum
Radius of Curvature
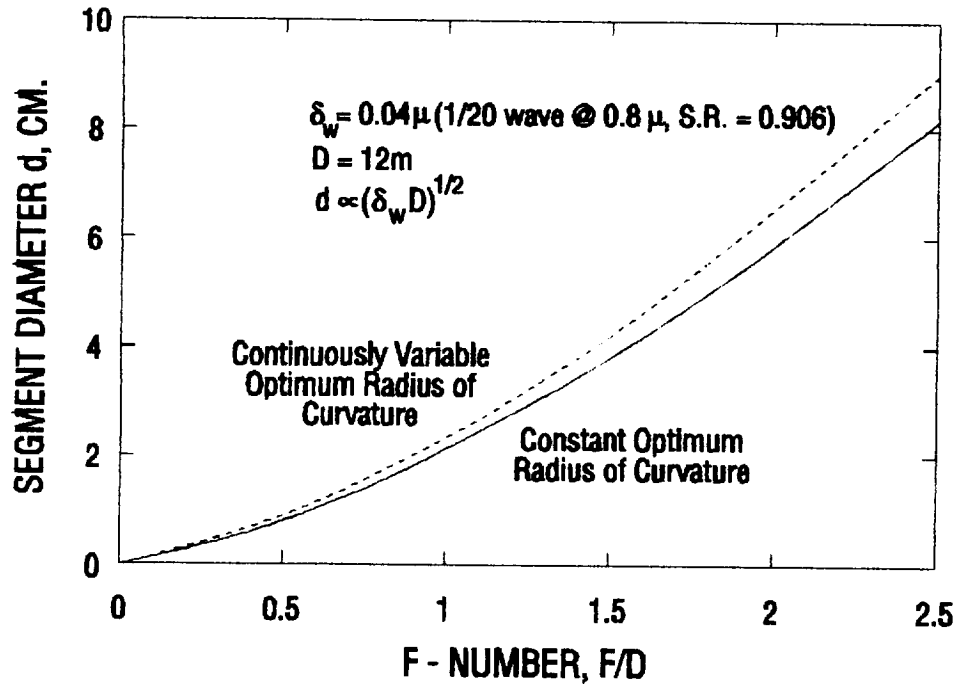
Fig. 1 Spherical-Figured Segment Requirements

$\delta_w = 0.04\mu$
$D = 12m$
$d \propto (\delta_w D)^{1/2}$

0°

30°

60°

Spherical

$\alpha = 1.0$
$\alpha = 0.8$
$\alpha = 0.5$
(inner / outer diameter
ratio of annulus)
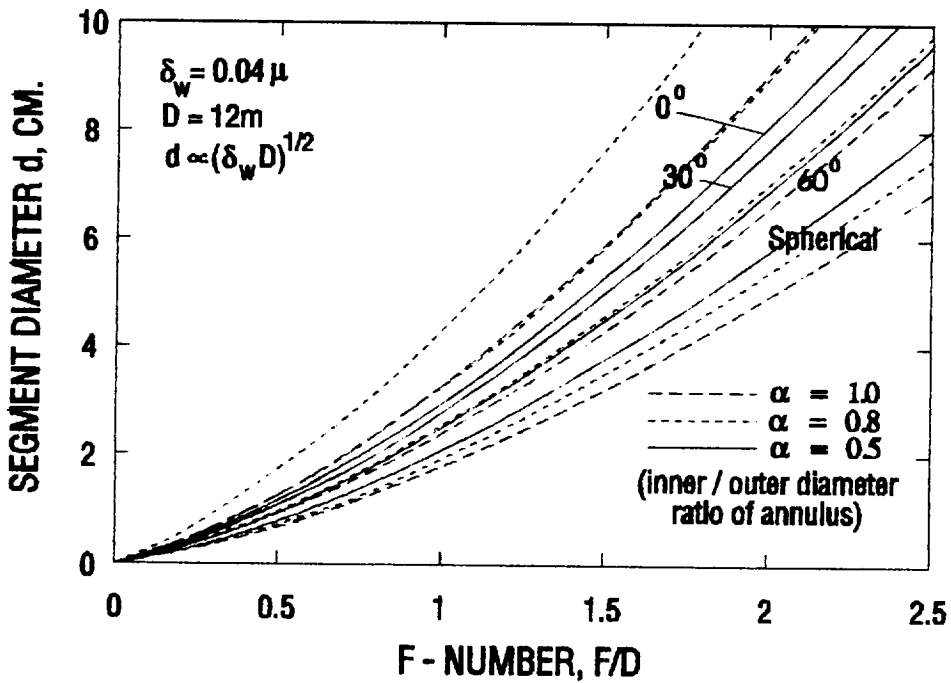
Fig. 2 Astigmatic Segment Requirements
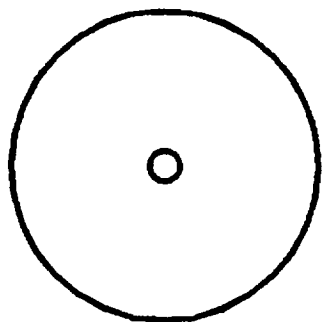
All Spherical
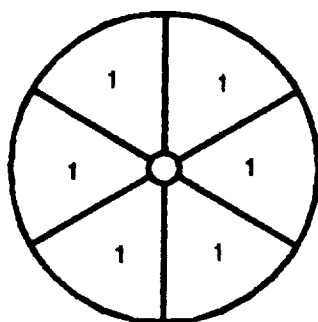
Identical Aspheres
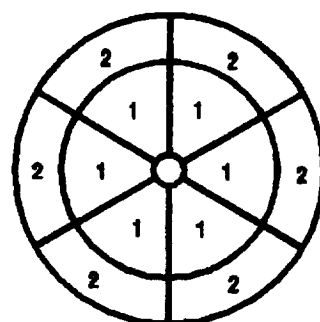
Two Aspheric Figures
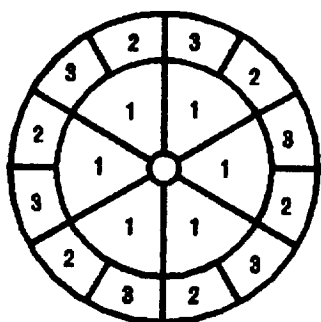
Two Aspheric Figures, Two Orientations in Outer Ring
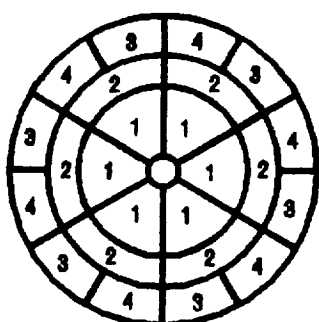
Three Aspheric Figures, Two Orientations in Outer Ring
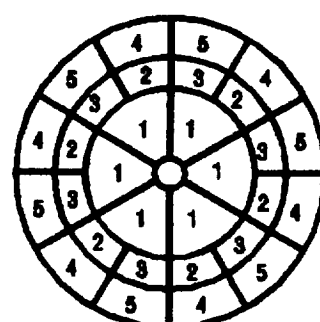
Three Aspheric Figures, Two Orientations in Each of Two Outer Rings
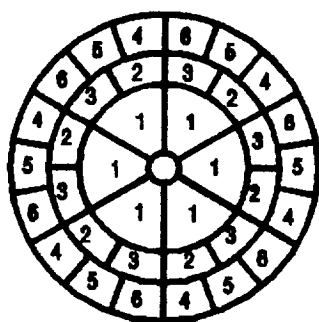
Three Aspheric Figures, Three Orientations in Outer Ring and Two in Middle

Fig. 3 Calculated Configurations

OPTIMUM SEGMENT FITTING TO A PARABOLIC SURFACE – PART II

Dr. Glenn W. Zeiders, The Sirius Group

A subject that continues to reappear in the SELENE program is the question of fitting hexagonal segments to a parabolic surface. This was briefly addressed at the 2/92 JPL Wavefront Sensing and Control Workshop by the author and in an analysis by D. Korsch who showed that non-interference could be assured by simply projecting and tilting the segments from the reference plane onto the paraboloid. However, because radial arcs lengthen while azimuthal ones remain unchanged under such a transformation, that simple fitting procedure produces increasingly large radial gaps away from the center while leaving essentially no azimuthal ones, and that can lead to unnecessarily large energy loss and, perhaps, difficulties in edge sensing. Here we begin with the same proposition, i.e. projecting the segments from the reference plane onto the curved surface, but we permit outward radial shifts to relieve the azimuthal "crunch", we specifically require that the gaps be locally symmetric (i.e., azimuthal = radial), and we consider the benefits of radial zones with slightly different-sized segments to close the gaps.

If we allow segments to be shifted outward by a distance $d(r)$ and to have an effective diameter $d(r)$, the mean azimuthal gap for segments initially at a distance r from the center is

$$\Delta_\theta = [2\pi(r+\delta) - Nd]/N, \quad Nd_o = 2\pi r \quad \Rightarrow \quad \Delta_\theta = (1 + \delta/r)\,d_o - d$$

and the radial gap between segments initially at r and those at $r + d_o$ is

$$\Delta_\rho = (r + \delta - d/2\cos\theta)_{r+do} - (r + \delta + d/2\cos\theta)_r = d_o + d_o\,{}^{D\delta}\!/_{Dr} - d_o\,\delta/r - d_o/2\,{}^{D}\!/_{Dr}(d\cos\theta)$$

where $\tan\theta = r/2F$, and where we have modeled the discrete segments by a continuous distribution, valid in the limit of very small segment size. Then, we find

$$\Delta_\rho - \Delta_\theta = d_o\,{}^{D\delta}\!/_{Dr} - d_o\,\delta/r + d/2\,(r/2F)^2 - d_o/2\,{}^{Dd}\!/_{Dr} + \langle small\ terms\rangle\,,$$

and we will henceforth let $\Delta = \Delta_\rho = \Delta_\theta$ to maintain local symmetry.

Case I: $\Delta = 0$ Letting $\delta = 0$ @ $r = D/2$, $d/d_o = \delta/r + 1 = \exp[(D^2/4 - r^2)/16F^2]$

which would require a continuous distribution of segment sizes for which the central segment would be 1.6% larger than those at the periphery for f/1.0.

Case II: $d = d_o$ Again with $\delta = 0$ @ $r = D/2$, $\delta/r = \Delta/d = (D^2/4 - r^2)/16F^2$.

This gives a maximum gap $\Delta = d\,(D/8F)^2$ @ $r = 0$, which is 625μ (0.025") for $d = 4$ cm and f/1.0, but this would reduce to 312μ if 4.031 cm segments were used within $r = D/\sqrt{2}$, and the gap would decrease further with increased zonal segmentation.

OPTIMUM GAUSSIAN TRUNCATION   G. W. Zeiders, The Sirius Group

The output beam from a free-electron laser tends to be a freely-propagating one with virtually no edge effects of edge-clipping, and that leads to an essentially infinite Gaussian profile which must be processed by the finite-sized transfer optics and the BTOS for final propagation to the target. Excessive power will be wasted if these elements truncate the beam at too small a radius, while excessive diffraction will occur if the truncation radius is too large, so an optimum ratio of beam/waist size occurs for which the peak far-field intensity (i.e., ideal Strehl ratio) is maximized.

The profile of an infinite gaussian beam is described by

$$ I = I_0 \exp\{-(r/a)^2/2\} \quad \text{so that} \quad P_\infty = 2\pi \int_0^\infty I\, r\, dr = 2\pi a^2 I_0 . $$

If the beam is truncated at a radius R, the peak far-field intensity is then proportional to

$$ [2 \int_{R\delta}^{R} r \sqrt{I}\, dr]^2 = [\sqrt{(P_\infty/2\pi a^2)} \int_{(R\delta)^2}^{R^2} \exp\{-(r/2a)^2\}\, dr^2]^2 $$

where $R\delta$ is the radius of the secondary mirror. Then, optimizing with respect to the beam/waist size ratio, we have (symbolically)

$$ y = [(\exp\{(\delta x)^2\} - \exp\{-x^2\})/x]^2 \quad (x = R/2a) $$

so that

$$ dy/dx = [2 x^2 (-\delta^2 \exp\{-(\delta x)^2\} + \exp\{-x^2\}) - (\exp[-(\delta x)^2\} - \exp\{-x^2\})] 2\sqrt{y}/x^2 , $$

is zero for optimum conditions, and this requires that

$$ (1 + 2 x^2) \exp\{-x^2\} = (1 + 2 \delta^2 x^2) \exp[-(\delta x)^2\}. $$

The resulting optimum beam size r/a, the Strehl ratio relative to a full ($\delta = 0$) infinite beam with the same waist size, and the fractional powers $1 - \exp\{-(\delta R/a)^2/2\}$ within the inner radius, $\exp\{-(R/a)^2/2\}$ beyond the outer [also the edge/center intensity ratio], and the net are shown in the table below as functions of δ:

d	0	0.05	0.10	0.15	0.20	0.25
R/a	2.2418	2.2355	2.2166	2.1870	2.1490	2.1046
Strehl	0.71533	0.71020	0.69501	0.67098	0.63967	0.57463
Inner Power	0	0.00623	0.02427	0.05239	0.08823	0.12926
Outer Power	0.08104	0.08219	0.08572	0.09149	0.09935	0.10919
Net Power	0.91896	0.91158	0.89001	0.85612	0.81242	0.76155

This corresponds to truncation slightly beyond the e^{-2} intensity points, and it might be expected that an optimization considering the cost of the telescope would result in a somewhat smaller value of R/a.

EOTV ORBITAL TRANSFER

Dr. Glenn W. Zeiders, The Sirius Group

In response to questions concerning the long Earth-orbital transfer times being reported, this report reviews some of the key principles that are important to the power beaming program. In the first part, the trajectory parameters for two-phase constant-acceleration thrusting from low orbit to a higher one are calculated, first tangential-directed for rapid energy addition, then normal-directed (constant energy) to meet the angular momentum requirement. The model is not meant to represent optimum conditions, but it does simulate an interesting flight profile, clearly shows the most important behavior, and gives some useful systems-level results:

1.   Continuous thrusting is far more costly than a Hohmann two-impulse, half-orbit transfer from the ΔV standpoint.

2.   Acceleration is probably the most important single factor determining the mission profile. The required ΔV increases only slightly with acceleration level, but mission duration decreases dramatically. High thrust and/or low weight are suggested to safely transit the Van Allen belts.

3.   At very low acceleration levels, the vehicle spirals slowly outward about the central body, and the radial velocity is sufficiently low that very little final maneuvering is required for injection into the new orbit. The overall ΔV can be shown to approach the difference of the two circular velocities, and this leads to a particularly simple closed-form solution which should prove useful for overall systems analysis as well as for interpretation of more detailed computer simulations.

In view of the preceding, the second part examines the requirements on the system specific weight and the specific impulse, and concludes that it is important that the former be reduced as much as possible, whereas the latter should be chosen judiciously with flight time in mind. High specific impulse saves propellant mass at the expense of thrust (acceleration), and, when the propellant mass becomes a small fraction of the total package (as it does at high I_s), the specific impulse may be able to be reduced significantly to dramatically reduce flight time without appreciably impacting overall system mass. Calculations for realistic conditions yield trip times considerably shorter than reported by Boeing.

---

1.   Continuous Thrusting Transfer

The planar equations of motion in polar coordinates and dimensionless form are

$$d^2 r / dt^2 - v^2 / r + 1/r^2 = a \cos \psi$$

$$d(r\, n) / dt = r\, a \sin \psi$$

where $\quad r = r / r_0 \qquad\qquad t = t \sqrt{\mu / r_0^3}$

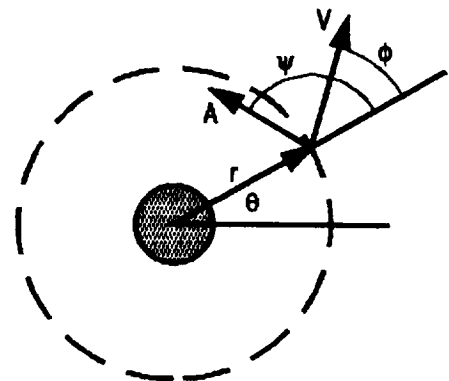$\qquad\quad v = V \sin \varphi \sqrt{r_0 / \mu} \qquad \alpha = A\, r_0^2 / \mu$

Fig. 1 Maneuver Geometry

and where the Earth gravitational constant $\mu = 3.9853 \cdot 10^5$ km^3 / sec^2. For transfer from low-Earth orbit (LEO) at 500 km altitude, the initial radius r_0 is 6878 km, and the other normalizing factors are $\sqrt{r_0^3/\mu} = 904$ sec $= 0.251$ hrs for time, $\sqrt{\mu/r_0} = 7.61$ km/sec for velocity, and $\mu/r_0^2 = 8.42$ m/sec^2 (0.860 G's) for acceleration.

r_F	a_T	r_T	t_T	q_T	a_N	t_N	q_N	$t_T + t_N$	$q_T + q_N$	$a_T t_T + a_N t_N$
6	.001	5.95	591	243	.0081	3.59	.258	595	243	.620
	.003	5.69	196	81.2	.0088	8.57	.604	205	81.8	.663
	.01	4.83	57.2	24.6	.0126	13.8	1.06	71.0	25.6	.746
	.03	3.45	17.6	8.55	.0194	16.3	1.48	33.9	10.0	.845
	.1	2.11	4.18	3.16	.0314	15.5	1.67	19.7	4.83	.904
	.3	1.18	1.21	1.31	.0347	16.3	2.49	17.6	3.80	.931
	1	1.02	.355	.414	.0352	16.7	3.03	17.1	3.45	.942
	Hohmann:							20.6	3.14	.499
5	.001	4.97	553	240	.0087	2.56	.238	555	240	.575
	.003	4.85	183	80.1	.0128	4.81	.441	188	80.5	.612
	.01	4.32	53.9	24.2	.0163	9.30	.904	63.2	25.1	.691
	.03	3.21	16.7	8.40	.0242	11.3	1.40	29.1	9.79	.780
	.10	2.01	4.00	3.10	.0410	11.8	1.60	15.8	4.70	.883
	.30	1.16	1.17	1.27	.0450	13.0	2.49	14.1	3.76	.933
	1.0	1.02	.342	.398	.0455	13.3	3.01	13.7	3.41	.950
	Hohmann:							16.32	3.14	.480
4	.001	3.99	500	234	.0110	1.49	.201	501	235	.516
	.003	3.93	166	78.2	.0168	2.82	.360	169	78.6	.546
	.01	3.68	49.1	23.6	.0244	5.18	.685	54.3	24.3	.617
	.03	2.88	15.5	8.15	.0307	8.67	1.30	24.2	9.44	.730
	.10	1.88	3.72	2.99	.0559	8.60	1.55	12.3	4.53	.852
	.30	1.14	1.11	1.21	.0600	9.89	2.47	11.0	3.68	.926
	1.0	1.01	.326	.377	.0607	10.3	2.99	10.6	3.37	.950
	Hohmann:							12.42	3.14	.449
3	.001	3.00	423	222	.0131	.849	.018	423	222	.434
	.003	2.99	141	74.1	.0745	.410	.080	141	74.2	.453
	.01	2.88	41.8	22.4	.0406	2.45	.496	44.2	22.9	.518
	.03	2.45	13.4	7.65	.0391	5.45	1.18	18.9	8.83	.616
	.10	1.69	3.30	2.80	.0800	5.73	1.47	9.03	4.27	.788
	.30	1.10	.995	1.09	.0829	7.08	2.48	8.08	3.57	.885
	1.0	1.01	.291	.332	.0839	7.46	2.98	7.75	3.31	.918
	Hohmann:							8.89	3.14	.393
2	.01	1.98	29.2	18.8	.0445	1.01	.370	30.2	19.2	.337
	.03	1.90	9.69	6.41	.0403	2.62	.983	12.3	7.39	.396
	.10	1.35	2.42	2.29	.1153	3.45	1.53	5.87	3.82	.640
	.30	1.05	.762	.830	.1103	4.66	2.56	5.42	3.39	.772
	1.0	1.00	.225	.250	.1113	5.00	2.98	5.23	3.23	.782
	Hohmann:							5.77	3.14	.284

TABLE I   CONTINUOUS THRUSTING ORBITAL TRANSFER

In-plane maneuvers are accomplished by appropriately programming the magnitude A and direction ψ of the acceleration, and this analysis specifically assumes constant tangential acceleration from a low circular orbit to the required final energy for a higher circular orbit, followed by constant normal acceleration to the required

angular momentum for the final orbit. In the first operation, the energy increases linearly with path length according to

$$E = V^2/2 - 1/\rho = \alpha_T S - 1/2 \;, \; S = \int V \, d\tau, \; \Delta S = (1 - r_0/r_F)/2\,\alpha_T,$$

and the trajectory is described by

$$\rho \, d^2\rho/dS^2 = (1 - 1/\rho \, V^2)[1 - (d\rho/dS)^2] \quad \text{where} \quad \rho = 1, V = 1, \text{ and } d\rho/dS = 0 \text{ @ } S = 0.$$

The trajectory for the second maneuver is described by

$$\rho \, d^2\rho/d\tau^2 = [1/\rho - 1/\rho_F - (d\rho/d\tau)^2] - \alpha_N \sqrt{[1 - (d\rho/d\tau)^2/(2/\rho - 1/\rho_F)]}$$

where the acceleration α_N required to match the boundary conditions can be shown to be given by

$$\sqrt{\rho_F} - H_T = 3\,\alpha_N\,\rho_F^{5/2}\,(\pi/4 - 2/3 - \sin^{-1}\sqrt{\rho_T/2\rho_F} + \{1 + 2/3\,\rho_T/2\rho_F\}\sqrt{\rho_T/2\rho_F}\sqrt{[1 - \rho_T/2\rho_F]})$$

where $H_T = \rho V \sqrt{[1 - (d\rho/dS)^2]}$ is the angular momentum at the end of the tangential-thrusting phase.

These equations have been numerically integrated on a PC, and the results are presented in Table I where the last three columns represent, respectively, the total normalized transit time, the total angular traverse (radians) about the central body, and the total normalized impulse. These quantities have in turn been plotted in Figure 2, and the corresponding dimensioned values are shown for a 500 km lower orbit (note that $\rho_F/\rho_0 = 6.1$ for a flight from LEO to GEO.) Also shown are the equivalent values for an ideal Hohmann transfer; they become substantially more favorable as the altitude change increases, but the maneuver requires infinite-acceleration
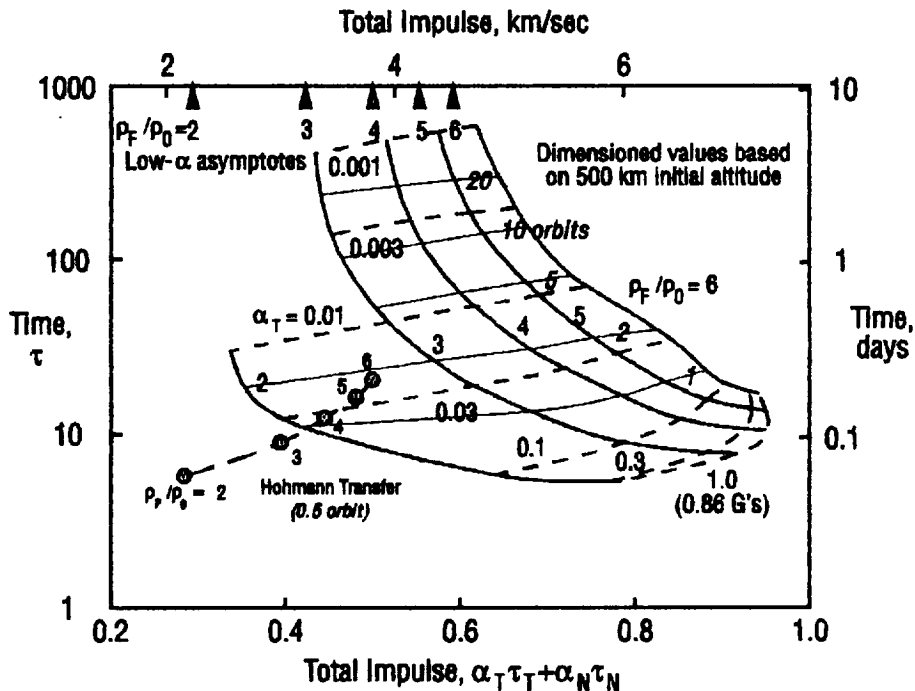

Fig.2 Orbital Transfer Requirements

impulses at the beginning and end of a half-orbit, and is not suitable for electric propulsion alone. The oscillations that may be noted in the results are probably not calculational artifacts, but rather are most likely due to the tendency of the vehicle to "hunt" about the mean trajectory; such behavior is clearly evident from the presence of the trigonometric functions in Benney's power series solution

$$\rho = 1 + 2\alpha (S - \sin S) + 4\alpha^2 [S^2 + S/2 (S \cos S - \sin S) + 2 (\cos S - 1)] + \ldots$$

for the case of constant tangential acceleration from a circular orbit.

It should be obvious from Figure 2 that the very long-duration missions being projected by Boeing reflect acceleration levels well below 0.001 and correspond to operation above the upper edge of the graph. For those conditions, the trajectory approaches a gradual spiral with many orbits around the central body, and simple closed-form results can be obtained in that case by noting that the velocity is essentially tangential and equal to the local circular value, i.e. $\rho V^2 \cong 1$. Thus,

$$2\alpha S \cong 1 - 1/\rho \quad \text{and} \quad \tau = \int dS / V \cong (1 - 1/\sqrt{\rho}) / \alpha$$

so that the velocity increment is just the difference between the initial and final orbital velocities, the vehicle spirals outward with

$$\rho \cong 1 / (1 - \alpha\tau)^2,$$

and the mission duration for a given orbit change is essentially inversely proportional to the acceleration.

These results should prove quite useful if one wishes to quantitatively examine the effects of laser propagation loss and/or intermittent thrusting as the vehicle passes through "irradiation cones." The geometry for the latter is shown in Figure 3, from which it follows that the exposure fraction at a particular altitude is given by

$$\varphi / \pi = [\theta - \sin^{-1}\{\sin\theta / (1 + h / R_0)\}] / \pi$$
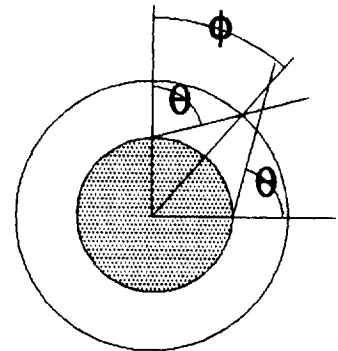
Fig. 3 Irradiation Geometry

for each ground station; this is plotted in Figure 4. The mean acceleration is proportional to the value, so the time spent near that altitude is inversely proportional to it. For a maximum angle of 60° from zenith, a vehicle at 500 km altitude would be accessible from each ground station 3.65% of the time (6.33% at 75°!), and it would rise to 6.40% at 1000 km and 10.42% at 2000 km. Although this matter will tend to heal itself as the program progresses and more ground stations become available, the real problem with low-acceleration transfer from LEO will remain: low altitudes where the radial velocity is the lowest (and the "masking" is the greatest) can also be the most lethal from the standpoint of the Van Allen radiation belts in which charged particles are trapped by the Earth's magnetic field. The inner belt, extending from the surface to about $2R_0$ and peaking at about $1.5R_0$ (3000-4000 km altitude), is composed primarily of penetrating protons of cosmic origin, whereas the outer belt, which extends nearly to GEO, is made up of low-energy electrons. A vehicle rising from LEO with constant tangential acceleration would spend at least 30% of its flight time in the more-dangerous lower radiation belt, and this certainly suggests the need for a high-thrust system to minimize the time spent at low altitudes, either using an initial kick from an auxiliary rocket or using a laser-propelled vehicle with power from relay satellites rather than from the surface and, perhaps, with degraded specific impulse to increase the thrust.

Acceleration is the key parameter determining mission duration, and short flight times will therefore require high thrust and/or low mass.

Fractional Coverage per Ground Station

0.2

No. of ground stations for 100% coverage = 6

8

Angle from zenith = 75° 70° 65° 60°

0.1

12

Van Allen proton flux peaks near 3000 km altitude, electron flux peaks near 15000 km and extends to near-GEO

0

0   1000   2000   3000

Altitude, km
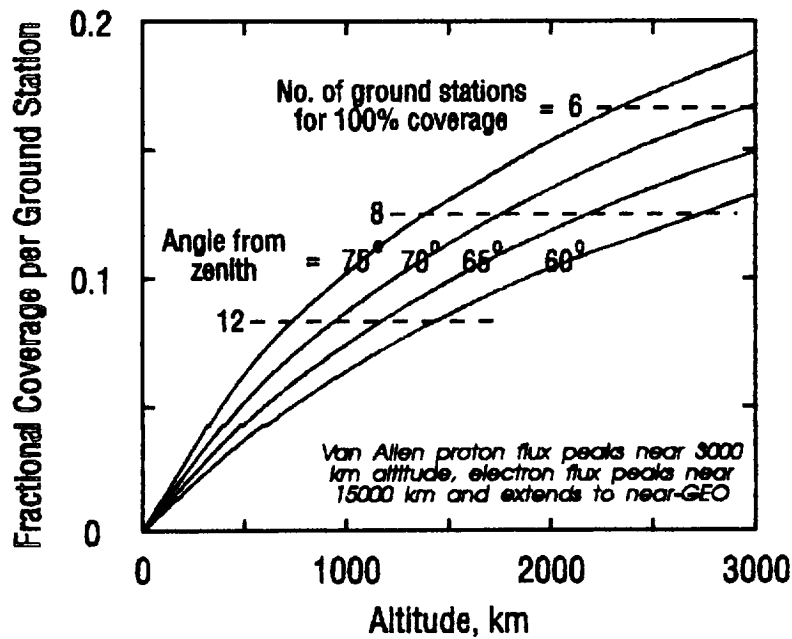
Fig.4 Coverage per Ground Station

2. Vehicle Considerations

The parameters of the vehicle are related by

$$F = m\, I_s\, g_0 \quad \text{and} \quad P_B = m v^2/2 = m\,(I_s\, g_0)^2/2 = F\, I_s\, g_0/2$$

where

F = thrust I_s = specific impulse

m = mass flow rate P_B = power in the thrust beam = $\eta\, P$.

Thus, $dv/dt = F/M = m\, dv/dm = F/(I_s\, g_0)\ dv/dm$,

which integrates to the familiar rocket equation

$$\Delta V = I_s\, g_0\ \ln(M_0/M) = I_s\, g_0\ \ln[1/(1 - M_{prop}/M_0)]$$

for constant specific impulse. Then, assigning a fixed mass M_{FIX} (payload, etc.) and individual time-dependent (shielding, etc.) and power-dependent masses M_{TIME} and M_{POWER}, the initial mass is given by

$$[M_{FIX} + (M_{POWER}/P)\ P]/M_0 = 1 - \{1 - \exp[-(\Delta V/I_s g_0)]\}\{1 + \{(M_{TIME}/\tau)\ (\Delta V)^2/(2P\eta)\}\ (I_s g_0/\Delta V)^2]$$

and the mission duration τ by

$$[M_{FIX} + (M_{POWER}/P)\ P]\ (\Delta V)^2/2P\eta\ /\ \tau = (\Delta V/I_s g_0)^2\ /\ \{\exp[(\Delta V/I_s g_0)] - 1\} - \{(M_{TIME}/\tau)\ (\Delta V)^2/(2P\eta)\}.$$

These results are plotted in Figure 5, from which it can be seen that the transfer time is minimized for $I_s g_0/\Delta V$ = 0.6275 (i.e., I_s < 300 seconds for all LEO/GEO transfers.) Although the curves for various values of the time-dependent mass parameter are interesting, their utility is limited because the parameter tends to be small; as a point of reference, using Grant Logan's shielding calculations presented at the 2/91 Beam Power Workshop at LeRC (2.5 tons for a 10 day transfer with 3.7 tons of propellant, I_s = 2500 sec, and ΔV = 4.3 km/sec), we find the parameter to be only 0.02. Nevertheless, the analysis is important because it shows that the gross weight (often used as a measure of overall performance for a space vehicle), varies weakly for large values of the specific impulse whereas the mission time varies essentially linearly with I_s in that region, so virtually any weighting of mission duration is likely to drive one to $I_s g_0/\Delta V$ = 2 - 3 for best operating conditions. To put Figure 5 in perspective with real parameters, consider the following:

I_s = 1200 sec. M_{POWER}/P = 5 kgm/kW

ΔV = 4.536 km/sec (500 km to GEO at low α) M_{FIX} = 2.5 tons

P = 500 kW with η = 0.5 M_{TIME} = 0.

Then, $I_s g_0/\Delta V$ = 2.593 M_{POWER} = 2.5 tons M_{PROP} = 2.35 tons M_0 = 7.35 tons

Δt = 7.53 days F = 42.5 newtonsF/$M_0 g_0$ = 0.0006

This is about twice as long as the minimum time – which would require substantially more propellant – and is only 47% heavier than would be achieved with infinite I_s – and infinite mission time.
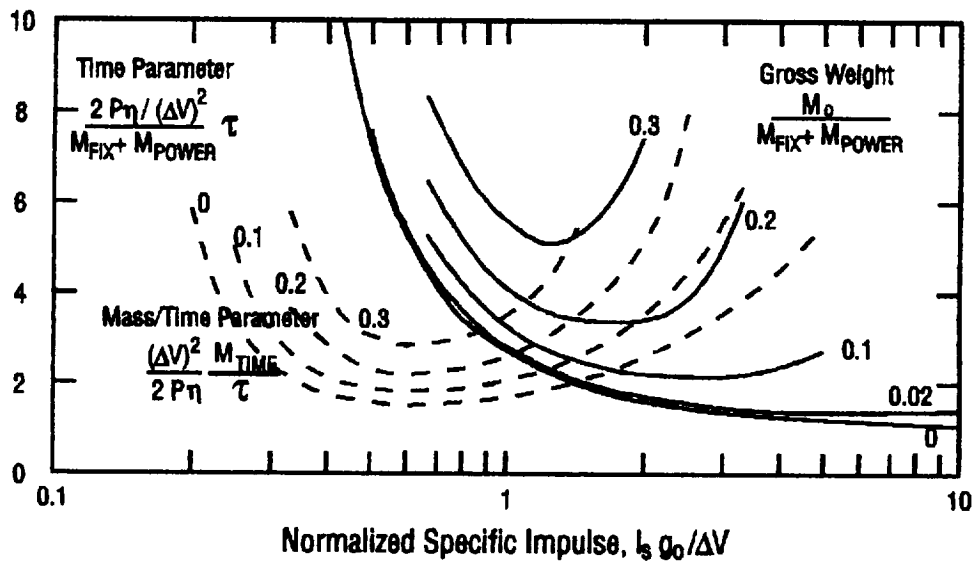
Fig. 5 Effects of Specific Impulse on Mission Duration and Goss Weight

Although not specifically plotted, one should note the effect of specific power M' = M_{POWER}/P in the equations. It always contributes negatiely by increasing the overall system mass, and it serves to limit the useful power to M_{FIX}/M'. For a fixed mass M_{FIX} of 2.5 tons, a value of M' = 5 kgm/kW would effectively limit the useful power to 500 kW, and 1 kgm/kW would be needed for 2.5 MW.

Increased specific impulse reduces propellant mass at the expense of thrust
(acceleration.) Once the propellant mass becomes a small fraction of the total
system, specific impulse may be reduced substantially to decrease mission time.

A lower value of specific power may be required to efficiently use the high
input power available with laser beaming.

D.6

ACTUATOR REQUIREMENTS FOR TURBULENCE COMPENSATION

Dr. Glenn W. Zeiders, The Sirius Group

A simple methodology, based on the work of Noll (Ref. 1) and Greenwood and Fried (Ref. 2), is presented for estimating the actuator requirements for adaptive optics correction of global tilt and residual piston error arising from Kolmogoroff atmospheric turbulence, and predictions are given for SELENE. The results of G&F for the frequency characteristics are specifically applied to ground-to-space conditions for which the segment sizes are very small compared to the full aperture, and results are given for several important crosswind distributions; it is found that the velocity profile has a strong effect on the power spectra and that high slew rates in particular significantly increase the required high-frequency response and accentuate the effects of high-altitude turbulence.

Atmospheric turbulence disturbs the air density and index of refraction along an optical path, large turbules primarily causing low-frequency centroid wander of the central diffractive lobe while small ones reduce the peak intensity, scattering energy over wide angles. The amount of wander and scatter for a uniform plane wave traversing a path along z through full-range Kolmogoroff turbulence are characterized by the scale

$$r_0 = \{0.423 \, k^2 \int C_n^2(z) \, dz\}^{-3/5}$$

where $k = 2\pi/\lambda$ is the wave number of the radiation; for the Hufnagel-Valley turbulence profile (Fig. 2) and a path inclined at an angle Θ from zenith, $r_0 = 11.1 \, \{\lambda_\mu^2 \cos \Theta\}^{3/5}$ cm where 73% of the contribution arises from the "ground layer" and only 9% is due to the "tropospheric spike." It is now well-known that appreciable improvement can be realized in both imaging and beaming applications if the disturbed wavefront is properly corrected over dimensions of r_0 or less. As long as the remaining distortion is not too large, the relative peak intensity (Strehl ratio) is reduced to $\exp(-<\sigma^2>)$ where $<\sigma^2>$ is the variance of the corrected wavefront from its mean.

Again for full-range Kolmogoroff turbulence with a plane wave and further assuming a uniformly-illuminated circular aperture of diameter D, Noll (Ref. 1) exactly evaluated the residual variances after progressive Zernike polynomials were removed, and showed that the mean variance for the "uncorrected" wavefront is

Piston-Corrected: $\qquad <\sigma^2>_P = 1.030 \, (D/r_0)^{5/3}$

after time-dependent piston is taken out to give zero mean (unnecessary in practice, but convenient for calculations), while the residual variance of a fully tilt-corrected wavefront is

Piston/Tilt-Corrected: $\qquad <\sigma^2>_{P/T} = 0.134 \, (D/r_0)^{5/3}$.

The tilt is equally probable in all directions, so the total time-averaged variance can be represented symbolically by $\delta^2 = a^2 + \theta^2 r^2$, and the spatially-averaged variance is then $<\delta^2> = (4/\pi D^2) \int 2\pi r \, \delta^2 \, dr = a^2 + \theta^2 D^2/8$. Thus, the variance of the tilt alone is

$$<\theta^2> = 1.792 \, (D/r_0)^{5/3} \, (\lambda/\pi D)^2$$

The aperture diameter in the above formulas is actually quite arbitrary, and the results can be applied equally well to the full A/O problem by using the full aperture size D to calculate $<\theta^2>$ for the global tilt corrector and the resulting wavefront variance $<\sigma^2>_{P/T}$ which is to be corrected by piston motion of the subapertures, while the tilt correction and resulting variance for a subaperture can be calculated with the same formulas by using its diameter d instead. Thus,

Tilt Mirror Requirement: $<\theta^2> = 0.182 \, (D/r_0)^{5/3} \, (\lambda/D)^2$

Subaperture Requirement: $<\sigma^2>_{P/T} = 0.134 \, (D/r_0)^{5/3}$ $<\theta^2> = 0.182 \, (d/r_0)^{5/3} \, (\lambda/d)^2$

Residual Wavefront Error: $<\sigma^2>_{P/T} = 0.134 \, (d/r_0)^{5/3}$.

so, in terms of allowable residual RMS wavefront error, the required subaperture size would be

δ_{RMS} :	$\lambda/5$	$\lambda/10$	$\lambda/20$	$\lambda/40$
Max. Strehl:	0.21	0.67	0.91	0.98
$(d/r_0)_{P/T\text{-CORRECTED}}$	4.39	1.91	0.83	0.36.

The primary advantage of global tilt removal is that large control displacements are required only at relatively low frequencies, whereas, were it not done, the high-frequency controls for the individual segments would have to be capable of mean strokes of $(1.030/0.134)^{0.5} = 2.77$ times that for residual correction alone, and the edge segments would have to move further yet. That may or may not be a problem; the cost/benefits of the separate global tilt correction system would depend upon the particular implementation, and would require a separate assessment based specifically upon it.

An ideal gaussian distribution is unbounded (although real effects will produce real limits in practice), so the translation from variance to full stroke tends to be a matter of individual choice, but the minimum realistic value to use as a base would appear to be $\sqrt{8}$, the reason being that it is the appropriate factor for a sine variation, i.e.

$$<\phi>^2 = \int_0^{2\pi} (\Phi/2 \sin\theta)^2 \, d\theta / 2\pi = \Phi^2 / 8,$$

and this should next be multiplied by "safety factor" of perhaps 1.5 - 2 to avoid "going up against the stops", then divided by another factor of two to account for the fact that phase is shifted by twice the displacement of a mirror upon reflection; thus, the overall multiplier would be 2.1 - 2.8 to go from root variance to P-P stroke (Lincoln Lab has consistently used 2.5 in the past, and it would seem appropriate to adopt that for SELENE as well.)

For a typical SELENE scenario for which the wavelength would be about 0.8μ to optimize the response from GaAs photovoltaic cells, the coherence scale size r_0 with Hufnagel-Valley turbulence would be 8.5 cm at zenith, but that would decrease to only 3.8 cm at 75°. The larger number of subapertures required for correction at large zenith angles could prove to be a very costly penalty to pay for increased angular coverage, and it is likely that a proper optimization might well call for higher laser power instead to provide the same delivery at reduced angle, but that is beyond the scope of this study, and a design value $r_0 = 4$ cm will henceforth be assumed here. Then, the RMS requirements for global tilt, piston, and subaperture tilt correction would be 3.30 μrad, 42.4 rad, and 8.53 μrad respectively for a 12 m aperture with 4 cm elements. Using the 2.5X multiplier, these would translate into P-P values of 4.1μ for edge stroke of a 1 m global tilt corrector (12X magnification), 13.5μ for piston, and 0.05μ for additional edge stroke of the piston to correct for subaperture tilt.

Spatial variations translate into temporal ones when the turbulence moves across the optical path (or vice versa), and the power spectrum measures the variance per unit frequency (radian^2/Hz) of the wavefront there. Greenwood and Fried (Ref. 2) showed that the power spectra of tilt and piston could be represented respectively by

$$F_\alpha(f) = 2.079 \, (\lambda/D)^2 \, (D/r_0)^{5/3} \, \{ \int C_n^2/f_0 \, H_\alpha(f/f_0) \, dz \} / \{ \int C_n^2 \, dz \}$$

and

$$F_\phi(f) = 2.079 \, (D/r_0)^{5/3} \, \{ \int C_n^2/f_0 \, H_\phi(f/f_0) \, dz \} / \{ \int C_n^2 \, dz \}$$

where $f_0 = V/\pi D$ is a function of the local crosswind velocity $V(z)$, and the H's are complicated integrals over the spatial region of interest. Their results showed that the segment diameter d has an influence only at high frequencies for which $f > f_0 \, D/d$, whereas segment location and overall tilt both govern the low-frequency behavior for $f < f_0$, overall tilt removal causing a significant reduction of the power densities there. With that in mind, they derived "single-point" asymptotic solutions for infinitesimally small segments (d = 0), both with and without prior global tilt removal, and then fit the data for finite element sizes with low-pass filter functions to approximately describe the rolloff at high frequencies due to integration over the extended transit times associated with finite d. The latter were found to be

$G_\alpha(y) = 1$, $y < 0.332$	$G_\phi(y) = 1$, $y < 0.366$
$= 1.12 - 0.361 \, y$	$= 1.26 - 0.712 \, y$
$= 0$, $y > 3.10$	$= 0$, $y > 1.77$

where $y = f/f_0 \, d/D = \pi f d/V$ is a function of the controlled segment size. In order of application for the case where global tilt is first removed, , the appropriate asymptotic single-point solution for "residual" tilt correction with the full aperture D being controlled is

$$H_\alpha(x) = (2\pi)^{-2} \, x^{-2/3} \, , \quad x = f/f_0$$

corresponding to global tilt left in, the appropriate solution for residual piston correction of the full aperture D using a control size d is

$$H_\phi(x) = 0.01037 \, x^{4/3} \quad \text{for } x < 2.216 \quad \text{(averaged over the region)}$$

$$= 0.25 \, x^{-8/3} \quad \text{for } x > 2.216$$

with global tilt removed, and the solution for final residual tilt correction by the subelements would be the same as for the overall tilt correction but with the subaperture size d used throughout as for the Noll variances. Note that the high-frequency tilt cutoff is essentially the inverse of the transit time across the control element as might be expected, and that the rapid $f^{-8/3}$ fall-off of the phase spectrum will cause the subelement size to have little effect on the overall residual phase variance (except for the high-frequency cutoff itself) when d << D. The full-range frequency integrals

$$\int F_\alpha(f) \, df = 1.81 \, (D/r_0)^{5/3} \, (\lambda/\pi D)^2 \quad \text{and} \quad \int F_\phi(f) \, df = 0.142 \, (D/r_0)^{5/3}$$

of the resulting expressions are in remarkably good agreement with Noll's exact calculations and serve to validate the approximations that were made.

Because of their dependence on f_o, the H's vary along the path when the crosswind velocity does, but, for the sake of generality, Greenwood and Fried chose not to perform the path integrations in their paper, rather ascribing their results to turbulence in a single "layer" and leaving it to the user to extend the analysis as needed to variable crosswind scenarios (Greenwood later performed the path integrations for the phase spectra for representative conditions in Ref. 3.) The path integration is absolutely necessary for SELENE, especially with the high slew rates associated with low-orbit applications, and this is facilitated by casting the spectra equations in the forms

$$F_\alpha(f) / \{(\lambda/D)^2 (D/r_o)^{5/3} D/V_{ref}\} = 2.079 [\{\int C_n^2/v^{1/3} dz\} + \{1.12\int C_n^2/v^{1/3} (1 - \beta/v) dz\}] / \{26.96 \beta^{2/3} \int C_n^2 dz\}$$
$$\text{for } v/\beta > 9.46 \qquad \text{for } 1 < v/\beta < 9.46$$

and
$$F_\phi (f) / \{(D/r_o)^{5/3} D/V_{ref}\} = 2.079 \beta^{4/3} [\{\int C_n^2/v^{7/3} dz\} + \{0.2475/\beta^4 \int C_n^2 v^{5/3} dz\}] / \{6.671\int C_n^2 dz\}$$
$$\text{for } v/\beta > 1.418 \qquad \text{for } v/\beta < 1.418$$

where $\beta = fD / V_{ref}$, $v = V / V_{ref}$ where V_{ref} is some convenient reference crosswind velocity, and where we have again neglected the high-frequency phase rollover. These have been evaluated numerically and are shown in Table I and Fig. 1 for the Hufnagel-Valley profile

$$C_n^2(h) = 5.94 \cdot 10^{-23} (W/27)^2 h^{10} exp(-h) + 2.7 \cdot 10^{-16} exp(-h/1.5) + 1.7 \cdot 10^{-14} exp(-10h) \; m^{-2/3} \quad (h \text{ in km})$$

$f D / V_{ref}$	Uniform Wind	Bufton Wind Profile		Slew	
		No Spike	Spike	No Spike	Spike
0.01	1.661	2.997	2.896	1.369	1.395
	0.00067	0.04333	0.03971	3.627	3.290
0.0316	0.7710	1.264	1.228	0.1884	0.2417
	0.00312	0.2011	0.1843	0.5814	0.5278
0.1	0.3579	0.2929	0.3004	0.02970	0.05939
	0.01446	0.9335	0.8556	0.1046	0.09647
0.3162	0.1272	0.00136	0.01074	0.00145	0.01281
	0.06714	0.08986	0.09441	0.01678	0.02242
1	0	0	0	2.3e-6	0.00089
	0.07713	0.00443	0.00870	0.00099	0.00856
3.162	0	0	0	1.6e-13	7.4e-10
	0.00358	0.00021	0.00040	4.6e-5	0.00045
10	0	0	0	0	0
	0.00017	9.5e-6	1.9e-5	2.1e-6	2.1e-5

Table I   Tilt and Piston Power Spectra for Kolmogoroff Turbulence
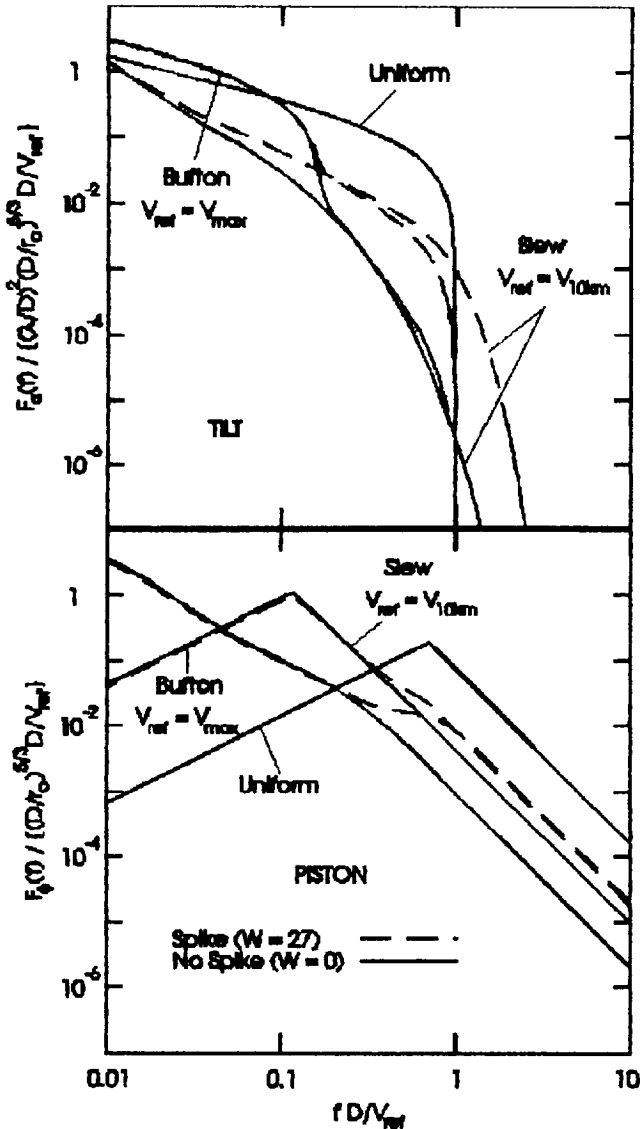
Fig. 1   Tilt and Piston Power Spectra with Global Tilt Removal

without (W = 0) and with (W = 27) the "tropospheric spike" and for the important cases of constant crosswind (*aka* Greenwood-Fried), the Bufton wind profile

$$V = 5 + 30\ exp[-((h-9.4)/4.8)^2]\ mps$$

with $V_{ref} = V_{max}$, and slew alone with V_{ref} equal to the velocity at 10 km; the profiles are shown for convenience in Fig. 2. The normalization using r_0 is such that the results are independent of the zenith angle and it is only the shape, not the absolute magnitudes, of the C_n^2 and velocity profiles that affect the results.
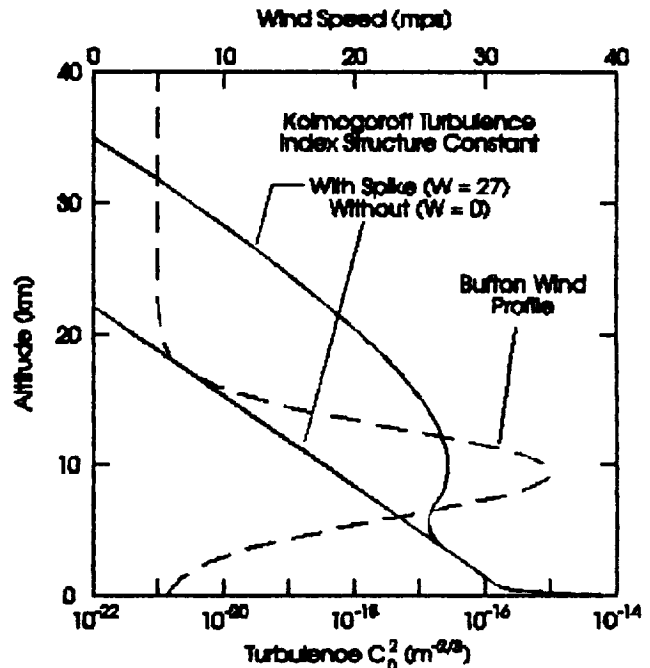
Fig. 2   Turbulence and Wind Profiles

Recalling that the tilt spectra vanish for $fD/V > 1$, there is no contribution beyond $fD/V_{ref} = 1$ for either the uniform or Bufton wind cases because each has a well-defined maximum velocity; the contribution to the Bufton tilt spectrum beyond $fD/V_{ref} = 1/7$ is due solely to its shear component in the tropospheric layer. The tilt spectrum for slew persists to high frequencies because the velocity rises continuously with altitude, but it, too, eventually vanishes at about $fD/V_{ref} = 1$ and 2 respectively as the high-altitude turbulence does at about 10 km without the spike and at about 20 km with it. The low-frequency spectra for the uniform and Bufton wind cases arises primarily from the strong turbulence in the ground layer, while that contribution is totally depressed with slew alone. The phase spectra shown for all the wind profiles persist to high frequencies where they decay as $f^{-8/3}$, but, had the rolloff been considered (as will be done shortly), they would also eventually vanish. The particular value of the "reference velocity" clearly has a significant effect on the spectral requirements, and it is important to put that in perspective for the slew case: if we consider an overhead path to a circular orbit with no earth rotation, the reference velocity would be

Orbital altitude, km:	300	1000	3000	10000	30000
Orbital velocity, mps:	7720	7340	6510	4930	3310
Reference velocity, mps:	257	73.5	21.7	4.93	1.10,

E.5

so, with typical natural winds, slew will totally determine the high-frequency spectra for beaming to low orbits, but it will otherwise have little influence. Composite cases can be modeled with sufficient accuracy for most purposes by superimposing and adding the appropriate curves with the proper reference velocities, then scaling their strength by keeping in mind that the integrals must satisfy the full-range frequency integrals -- which are totally independent of crosswind conditions.

By definition, the integrals under the spectral curves are the contributions to the variances in that frequency integration interval, so, following Greenwood (Ref. 3), the residuals after correction up to a high-frequency cutoff f_c for closed-loop servo systems with binary (sharp-edged) and a more realistic RC response are given by

$$\sigma_r^2 = \int F(f)\, H(f / f_c)\, df$$

where

$$H(f / f_c) = 0 \text{ for } f < f_c,\ 1 \text{ for } f > f_c \quad \text{(Binary)}$$

$$H(f / f_c) = f^2 / [f^2 + f_c^2] \quad \text{(RC)}$$

are the power rejection response functions; note that the low-frequency limit will generally be DC. Both the tilt and piston high-frequency rolloffs are important at the conditions of interest, and the resulting residuals are shown in Fig. 3 where, in all cases, d should be considered to be the size of the appropriate control element. An interesting analytic solution can be obtained when the spectra F(f) can be represented by a power law of the form f^{-n}, and it can then be shown that the binary cutoff is related to the residual variance by $F(r_0 f_c/V_{ref})\, r_0 f_c/V_{ref} = (n - 1)\, \sigma_r^2$ and that the RC cutoff frequency exceeds the binary value by a factor of $[\pi(n - 1)/2] / \sin[\pi(3 - n)/2]$ for a given residual; the cutoffs for this case are intrinsically independent of any mirror diameter for a given r_0, and the cutoff ratio is 2.62 for n = 8/3.

Although there is little advantage to be gained by compensating global tilt to much less than a diffraction angle for almost any laser beaming application, the value on the ordinate of the global tilt plot will still have to be no more than about $(r_0/D)^{5/3}$; this will usually be less than about 10^{-3} for most short-wavelength ground-to-space situations, so the variance will decrease rapidly with relatively small increases of cutoff frequency and can be made to essentially vanish with little cost penalty. Furthermore, except for beaming to low orbits, the transit time across the beam will generally be large enough that the cutoff frequency for global tilt control will be relatively small, typically just a few Hz, but caution is advised because the steepness of the curves is "a two-edged sword", and insufficient response can produce a dramatic increase in centroid wander to the point that the beam becomes useless. For correction over the scale of a subaperture, d/r_0 will be close to unity for both piston and tilt, so the tilt ordinate should be about 0.01 or less ($\lambda/20$ RMS at the edge) while the piston should be less than about 0.1 (90% Strehl), and close examination of Fig. 3 then suggests that the two give about the same result. The resulting frequencies will be much larger, potentially
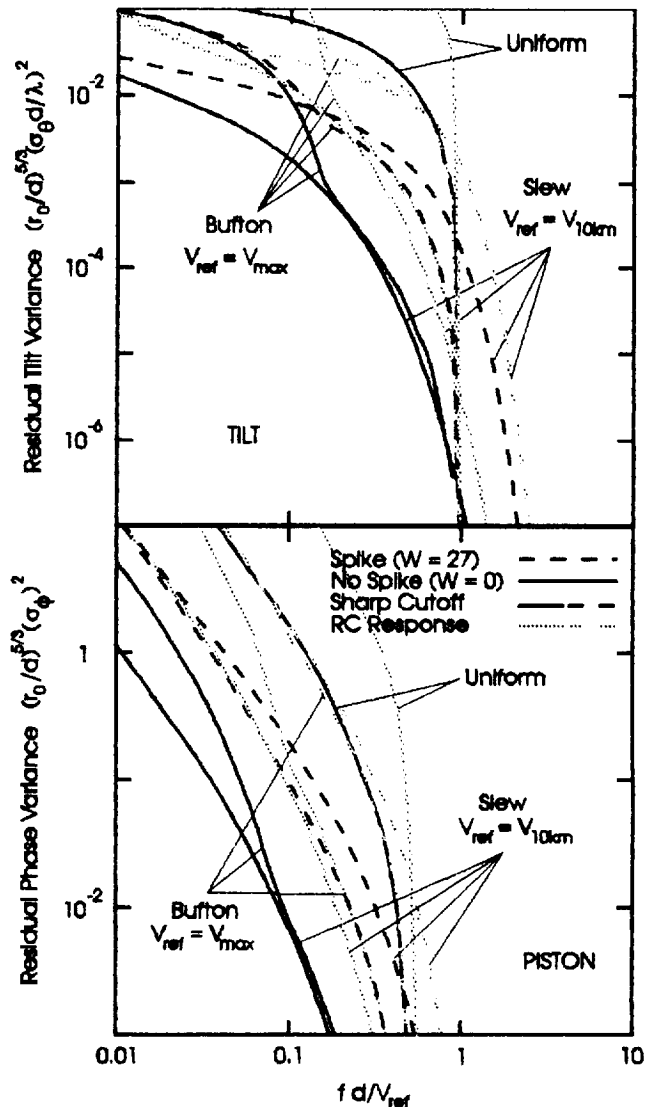
Fig. 3   Residual Variances

several KHZ with low-orbit beaming, than those for global tilt because the relevant transit time will be that over the much smaller subaperture, and the warning about insufficient response bears repeating here because errors in this case will produce small-spatial-scale disturbances that scatter the energy over wide angles. It should be noted that, although the crosswind V_θ for off-zenith conditions is related to the zenith wind V_0 by

$$(V_\theta / V_0)^2 = 1 - [\sin\theta / (1 + h/R_E)]^2, \quad R_E = 6370 \text{ KM},$$

and that this will tend to compensate somewhat for the smaller r_0 there, the high-frequency requirements will be primarily determined by the minimum transit time, and that should be evaluated with the diameter d equal to the minimum r_0 (i.e., the off-zenith value which defines the required subaperture size) and with the maximum velocity that will be encountered (i.e., that at zenith.)

Turning again to SELENE with $D = 12$ m and $d = r_{06} = 4$ cm, it is useful to consider two cases, one with beaming only to high orbits where the velocity would be given by the Bufton profile ($V_{ref} = 35$ mps), and the other for beaming to a 300 km orbit for which slew would be dominant ($V_{ref} = 257$ mps). Then, using RC servo response with the spiked turbulence profile and with $\sigma_6 = 0.5$ λ/D, the normalized residual tilt variance would be $(r_0/D)^{5/3}(\sigma_6 D/\lambda)^2 = 1.8 \cdot 10^{-5}$, and the corresponding cutoff frequencies would be 2.9 HZ ($fD/V_{ref} = 1$) and 39 HZ ($fD/V_{ref} = 1.8$) respectively. Basing the subaperture requirements on $\sigma_\phi^2 = 0.1$ and $\sigma_6 = \lambda/10d$ as before but with $r_{00} = 8.5$ cm (the zenith value), the normalized tilt and phase variances of 0.035 and 0.35 give essentially the same requirements, 130 HZ for the high-orbit system ($fd/V_{ref} = 0.15$) and 1350 HZ for the low ($fd/V_{ref} = 0.21$.)

Low-orbit applications clearly impose extremely severe requirements on the AO system (and, of course, on the slew mechanism), so a shared system with a much smaller dedicated beam director -- which would be effective at short ranges -- might prove optimum for beaming to LEO with far fewer high-frequency elements. For example, a 2.4 meter telescope operating at 0.8μ will produce a 2.4 m spot at 3000 km range, and this will require only 3600 4 cm elements as compared to the 90000 elements in a 12 m system -- all of which would have to respond at high frequency! Although the global tilt control of the smaller system would have to respond to about 180 HZ, the required throws of all of the actuators would be about 4X smaller, and the larger system could be designed for the less-stressing high-orbit applications alone.

---

1.   R. J. Noll, "Zernike polynomials and atmospheric turbulence", JOSA 66(3), pp. 207-211 (1976)

2.   D. P. Greenwood and D. L. Fried, "Power spectra requirements for wave-front-compensative systems," JOSA 66(3), pp. 193-206 (1976)

3.   D. P. Greenwood, "Bandwidth specification for adaptive optics systems," JOSA 67(3), pp. 390-393 (1977)

DETERMINISTIC CONTROL OF HEXAGONAL SEGMENTED MIRRORS

Dr. Glenn W. Zeiders, The Sirius Group

Equations are presented for the control of hexagonal segmented mirrors based on the approach recently suggested by Enguehard and Hatfield (Ref. 1), examples are given to illustrate the technique, and comments are offered on its use.

To review the basics of the AMP approach, consider an array of segments with mid-point edge differences

$$d_{ij} = U_i - U_j - (t_i + t_j)_k / 2,$$

where U_i is the centerline piston displacement of segment i and t_{ik} is the edge tilt displacement of the particular edge. We can then identify loops about each of the inner vertices through the mid-points and about any internal "holes", and it can be shown easily that the loops will be independent if each is minimized and passes only through segment boundaries that are internal to the surface. The sum f_i of the edge differences around each such loop is independent of the piston displacements and depends only upon the neighboring tilts, so, since the tilts are the sole measureables with a Shack-Hartmann sensor and are the only knowns at the start of the computation, the f's may be regarded as constants. Seeking as AMP did to minimize the sum of the squares of all of the mid-point edge differences, subject to the constraints that each f_i is constant for a given set of tilt measurements, the optimization problem can be expressed as

$$(\delta/\delta d_i) \{ \sum d_i^2 - \lambda \cdot f \} = 0,$$

thereby associating an element of a new vector λ with each element of f, the elements of λ (each associated with a different loop) being given by

$$2d_i = \sum \lambda_j \quad \text{or} \quad 2d = M_2 \cdot \lambda$$

where the summation extends only over those loops actually crossing the particular edge. Substituting the latter in the equations for f, we obtain

$$2f = M_1 \cdot \lambda,$$

so that the "optimum" edge displacements are related to the tilts by the linear transformation

$$d = (M_2 \cdot M_1^{-1}) \cdot f,$$

which then directly gives the piston displacements through the first set of equations. The two M matrices -- and, most importantly, the matrix product $M_2 \cdot M_1^{-1}$ -- are totally predetermined by the array geometry and do not depend on the atmospheric distortion, so the transformation need be accomplished only once and can be realized in hard-wired circuitry.

To apply the approach to hexagonal segmented mirrors, consider the nomenclature defined by the figure at the right and by

$$d_{i,j\,A} = U_{i,j+1} - U_{i,j} - (t_{i,j+1} + t_{i,j})_A / 2$$

$$d_{i,j\,B} = U_{i+1,j} - U_{i,j} - (t_{i+1,j} + t_{i,j})_B / 2$$

$$d_{i,j\,C} = U_{i+1,j-1} - U_{i,j} - (t_{i+1,j-1} + t_{i,j})_C / 2$$
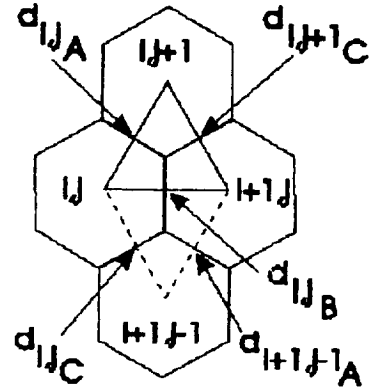
where the tilts in the triangular frame are related to Cartesian ones by

$$t_A = (t_x + \sqrt{3}\,t_y)/2, \quad t_B = t_x, \quad t_C = (t_x - \sqrt{3}\,t_y)/2$$

Thus, traversing the triangular loops in the clockwise direction, the constraint relations become

$$f_{i,j} = d_{i,j\,A} - d_{i,j\,B} + d_{i,j+1\,C} = -(t_{i,j+1} + t_{i,j})_A/2 + (t_{i+1,j} + t_{i,j})_B/2 - (t_{i+1,j} + t_{i,j+1})_C/2$$

$$= [\sqrt{3}\,(t_{i+1,j} - t_{i,j})_y + (t_{i+1,j} + t_{i,j} - 2t_{i,j+1})_x]/4$$

and

$$f'_{i,j} = -d_{i+1,j-1\,A} + d_{i,j\,B} - d_{i,j\,C} = (t_{i+1,j} + t_{i+1,j-1})_A/2 - (t_{i+1,j} + t_{i,j})_B/2 + (t_{i+1,j-1} + t_{i,j})_C/2$$

$$= [\sqrt{3}\,(t_{i+1,j} - t_{i,j})_y - (t_{i+1,j} + t_{i,j} - 2t_{i+1,j-1})_x]/4,$$

and the result of the differentiation is

$$2 d_{i,j\,A} = \lambda_{i,j} - \lambda'_{i-1,j+1}$$

$$2 d_{i,j\,B} = -\lambda_{i,j} + \lambda'_{i,j}$$

$$2 d_{i,j\,C} = \lambda_{i,j-1} - \lambda'_{i,j}$$

considering only triangular loops about internal vertices; λ terms that correspond to "open" loops at the external boundaries will vanish, and terms at inner boundaries will be replaced by ones for the longer loops used to encircle holes in the array. Substituting the above in the equations for f and f', we obtain

$$2 f_{i,j} = 3\lambda_{i,j} - \lambda'_{i-1,j+1} - \lambda'_{i,j+1} - \lambda'_{i,j}$$

$$2 f'_{i,j} = 3\lambda'_{i,j} - \lambda_{i,j-1} - \lambda_{i,j} - \lambda_{i+1,j-1},$$

each of which effectively averages the primary triangular path with its three nearest neighbors – and enables relatively easy construction of the M_1 and M_2 matrices as shown below. If segment i,j were to be removed, the

	$\lambda_{i,j-1}$	$\lambda_{i+1,j-1}$	$\lambda_{i,j}$	$\lambda'_{i,j}$	$\lambda'_{i-1,i+1}$	$\lambda'_{i,j+1}$
$2f_{i,j}$			3	-1	-1	-1
$2f'_{i,j}$	-1	-1	-1	3		
$2d_{i,j\,A}$			1		-1	
$2d_{i,j\,B}$			-1	1		
$2d_{i,j\,C}$	-1			1		

F.2

equations for $f_{i-1,j}$, $f_{i-1,j+1}$, $f_{i,j}$, $f_{i,j}$, $f_{i,j-1}$, and $f_{i-1,j}$ would be replaced with the single equation

$$2\,f_H = 6\lambda_H - \lambda'_{i-2,j+1} - \lambda_{i-1,j+1} - \lambda'_{i,j+1} - \lambda_{i+1,j} - \lambda'_{i,j-1} - \lambda_{i-1,j-1},$$

for the six-sided loop around the hole, the edge differences $d_{i,j\,A}$, $d_{i,j\,B}$, $d_{i,j\,C}$, $d_{i-1,j\,A}$, $d_{i-1,j\,B}$, and $d_{i-1,j\,C}$ would vanish, and those for $d_{i-1,j\,A}$, $d_{i-1,j+1\,B}$, $d_{i,j+1\,C}$, $d_{i+1,j-1\,A}$, $d_{i,j-1\,B}$, and $d_{i-1,j\,C}$ would be replaced with

$$2\,d_{i-1,j\,A} = \lambda_H - \lambda'_{i-2,j+1} \qquad 2\,d_{i-1,j+1\,B} = \lambda_H - \lambda_{i-1,j+1} \qquad 2\,d_{i,j+1\,C} = \lambda_H - \lambda'_{i,j+1}$$

$$2\,d_{i+1,j-1\,A} = \lambda_{i+1,j-1} - \lambda_H \qquad 2\,d_{i,j-1\,B} = \lambda'_{i,j-1} - \lambda_H \qquad 2\,d_{i-1,j\,C} = \lambda_{i-1,j-1} - \lambda_H.$$

A representative set of loops and the corresponding M_1 and M_2 matrices are shown in Fig. 1 for a 19-element filled array, and the solution matrices M_1^{-1} and $M_2 \cdot M_1^{-1}$ are given in Fig. 1a. Only five types of mating edges are possible with a 19-element filled array, and these are shown in Fig. 1a with the corresponding weighting functions from $M_2 \cdot M_1^{-1}$; as an aid to visualizing the extent of the interactions, loops whose weights exceed 10% of the maximum are shaded, and those which exceed 20% are the darker. Equivalent results for the same array with a missing central element are shown in Figs. 2 and 2a for comparison (there are only four types of mating edges with that geometry.) Although the input matrices are quite sparse, the solution ones are not, and the results show that the influence generally extends well beyond the nearest neighbors, suggesting that convergence problems might be encountered with an iterative solution. Note in particular that the missing segment actually causes the influence to be more widely spread, causing further problems for iteration while having no negative impact on the deterministic solution.

This advantage of the AMP approach is that it is deterministic and not iterative, but its success depends upon the ability to establish a reference surface from which piston displacements can be measured. Although the predicted edge differences can in theory be used to individually adjust the segments (or each be combined with the local average tilt to give the piston differential across the gap), the differences are likely to be so small that measurement errors will accumulate excessively, and they should be used instead in groups to specify piston displacements from a common reference piston – *not each with reference to a nearest neighbor*. The flexible telescope structure being pursed for SELENE appears to preclude an overall mechanical reference for piston displacement, and the atmospheric distortions from the "beacon" prevent it from being an optical reference; similarly, the edge measurement techniques that have been proposed may not be sufficiently accurate to prevent an unacceptable error buildup across the beam if edge displacements were to be used throughout. However, a "hybrid" system (woofer/ midrange/tweeter) using the flexible substructure with rigid multi-element segments, either interferometric or edge-referenced, might provide a workable compromise. Otherwise it appears that an "invention'" will be required to provide the required reference.

A second key question of the importance of the analysis is, of course, whether minimization of the mid-point edge differences really represents the optimum condition. It clearly does not offer the precision of a wavefront-matching approach such as that claimed by JPL, but it's a physically realistic one, and it deserves to be tested, probably via a Zernike analysis against a more rigorous approach, to see which offers the greatest cost benefit. It should be kept in mind that AMP made no claim that the mid-point matching condition was indeed the best one, but they chose to use it since it should be near-optimum and since it had already been accepted as an optimizing condition by KAMAN and others. Their approach could probably be modified to accept a better premise should one be offered.

1.   S. Enguehard and B. Hatfield, "Minimizing Edge Misalignments for Segmented Mirror Adaptive Optics," AMP-92-10 (1992)

M1

	20	30	11'	21'	31'	11	21	31	02'	12'	22'	32'	02	12	22	32	03'	13'	23'	03	13	23	04'	14'
20	(3)	0	-1	-1	0	0	0	0	0	0	0	0	0	0	0	0	0	0	0	0	0	0	0	0
30	0	(3)	0	-1	-1	0	0	0	0	0	0	0	0	0	0	0	0	0	0	0	0	0	0	0
11'	-1	0	(3)	0	0	-1	0	0	0	0	0	0	0	0	0	0	0	0	0	0	0	0	0	0
21'	-1	-1	0	3	0	0	-1	0	0	0	0	0	0	0	0	0	0	0	0	0	0	0	0	0
31'	0	-1	0	0	(3)	0	0	-1	0	0	0	0	0	0	0	0	0	0	0	0	0	0	0	0
11	0	0	-1	0	0	3	0	0	-1	-1	0	0	0	0	0	0	0	0	0	0	0	0	0	0
21	0	0	0	-1	0	0	3	0	0	-1	-1	0	0	0	0	0	0	0	0	0	0	0	0	0
31	0	0	0	0	-1	0	0	3	0	0	-1	-1	0	0	0	0	0	0	0	0	0	0	0	0
02'	0	0	0	0	0	-1	0	0	(3)	0	0	0	-1	0	0	0	0	0	0	0	0	0	0	0
12'	0	0	0	0	0	-1	-1	0	0	3	0	0	0	-1	0	0	0	0	0	0	0	0	0	0
22'	0	0	0	0	0	0	-1	-1	0	0	3	0	0	0	-1	0	0	0	0	0	0	0	0	0
32'	0	0	0	0	0	0	0	-1	0	0	0	(3)	0	0	0	-1	0	0	0	0	0	0	0	0
02	0	0	0	0	0	0	0	0	-1	0	0	0	(3)	0	0	0	-1	0	0	0	0	0	0	0
12	0	0	0	0	0	0	0	0	0	-1	0	0	0	3	0	0	-1	-1	0	0	0	0	0	0
22	0	0	0	0	0	0	0	0	0	0	-1	0	0	0	3	0	0	-1	-1	0	0	0	0	0
32	0	0	0	0	0	0	0	0	0	0	0	-1	0	0	0	(3)	0	0	-1	0	0	0	0	0
03'	0	0	0	0	0	0	0	0	0	0	0	0	-1	-1	0	0	3	0	0	-1	0	0	0	0
13'	0	0	0	0	0	0	0	0	0	0	0	0	0	-1	-1	0	0	3	0	0	-1	0	0	0
23'	0	0	0	0	0	0	0	0	0	0	0	0	0	0	-1	-1	0	0	3	0	0	-1	0	0
03	0	0	0	0	0	0	0	0	0	0	0	0	0	0	0	0	-1	0	0	(3)	0	0	-1	0
13	0	0	0	0	0	0	0	0	0	0	0	0	0	0	0	0	0	-1	0	0	3	0	-1	-1
23	0	0	0	0	0	0	0	0	0	0	0	0	0	0	0	0	0	0	-1	0	0	(3)	0	-1
04'	0	0	0	0	0	0	0	0	0	0	0	0	0	0	0	0	0	0	0	-1	-1	0	(3)	0
14'	0	0	0	0	0	0	0	0	0	0	0	0	0	0	0	0	0	0	0	0	-1	-1	0	(3)

M2

	20	30	11'	21'	31'	11	21	31	02'	12'	22'	32'	02	12	22	32	03'	13'	23'	03	13	23	04'	14'
22A	0	0	0	0	0	0	0	0	0	0	0	0	0	1	0	0	-1	0	0	0	0	0	0	0
23C	0	0	0	0	0	0	0	0	0	0	0	0	0	1	0	0	0	-1	0	0	0	0	0	0
23B	0	0	0	0	0	0	0	0	0	0	0	0	0	0	0	0	1	0	0	-1	0	0	0	0
23A	0	0	0	0	0	0	0	0	0	0	0	0	0	0	0	0	0	0	0	0	1	0	-1	0
24C	0	0	0	0	0	0	0	0	0	0	0	0	0	0	0	0	0	0	0	0	1	0	0	0

Figure 1   19-Element Hexagonal Array

INV(M1)

A large square numerical matrix (inverse of M1) with row and column labels: 2Θ, 3Θ, 1'', 2'', 3'', 11, 21, 31, θ2, 12, 22, 32, θ2, 12, 22, 32, θ7, 17, 27, θ3, 13, 23, θ4, 14. The body contains densely-printed decimal coefficient values which are not legibly resolvable.

M2*INV(M1)

	2Θ	3Θ	1''	2''	3''	11	21	31	θ2	12	22	27	θ2	12	22	32	θ7	17	27	θ3	13	23	θ4	14
22A	0.00536	0.01724	-0.00536	0.02144	0.03027	-0.02144	0.04173	0.07308	-0.01724	-0.04173	0.14548	0.04498	-0.03027	-0.14548	0.32114	0.05136	-0.07308	-0.32114	0.13909	-0.04498	-0.13909	0.03477	0.05136	-0.03477
22C	0.02491	0.02774	0.02260	0.05213	0.03108	0.04289	0.10375	0.06551	0.02260	0.08346	0.17955	-0.01021	0.02491	0.10375	0.25771	-0.08613	0.05213	0.17955	-0.27618	0.02774	0.06651	-0.08613	0.03108	-0.01021
22B	0.01415	0.01981	0.01167	0.03059	0.02983	0.02144	0.05762	0.06969	0.01073	0.04173	0.10112	0.07012	0.01076	0.04594	0.17666	0.14368	0.02154	0.07454	0.36091	0.00793	-0.00118	-0.23981	0.00225	-0.09033
22A	0.00076	0.00302	-0.00076	0.00305	0.00602	-0.00305	0.00536	0.01505	-0.00302	-0.00536	0.01839	0.02073	-0.00602	-0.01839	0.03477	0.04714	-0.01905	-0.03477	0.12070	0.02073	-0.12070	0.28017	-0.04714	-0.28017
24C	0.01339	0.01678	0.01263	0.02754	0.02281	0.02449	0.05245	0.05164	0.01376	0.04709	0.08273	0.04939	0.01678	0.06433	0.11408	0.09654	0.03659	0.10831	0.24021	0.02866	0.11952	0.48002	0.04939	0.19985

Figure 1a   19-Element Hexagonal Array Solution

F.5

M1

	20	30	11'	21'	31'	11	31	02'	32'	H	02	32	03'	23'	03	13	23	04'	14'
20	3	0	-1	-1	0	0	0	0	0	0	0	0	0	0	0	0	0	0	0
30	0	3	0	-1	-1	0	0	0	0	0	0	0	0	0	0	0	0	0	0
11'	-1	0	(3)	0	0	-1	0	0	0	0	0	0	0	0	0	0	0	0	0
21'	-1	-1	0	3	0	0	0	0	0	-1	0	0	0	0	0	0	0	0	0
31'	0	-1	0	0	(3)	0	-1	0	0	0	0	0	0	0	0	0	0	0	0
11	0	0	-1	0	0	3	0	-1	0	-1	0	0	0	0	0	0	0	0	0
31	0	0	0	0	-1	0	3	0	-1	-1	0	0	0	0	0	0	0	0	0
02'	0	0	0	0	0	-1	0	(3)	0	0	-1	0	0	0	0	0	0	0	0
32'	0	0	0	0	0	0	-1	0	(3)	0	0	-1	0	0	0	0	0	0	0
H	0	0	0	-1	0	-1	-1	0	0	6	0	0	-1	-1	0	-1	0	0	0
02	0	0	0	0	0	0	0	-1	0	0	(3)	0	-1	0	0	0	0	0	0
32	0	0	0	0	0	0	0	0	-1	0	0	(3)	0	-1	0	0	0	0	0
03'	0	0	0	0	0	0	0	0	0	-1	-1	0	3	0	-1	0	0	0	0
23'	0	0	0	0	0	0	0	0	0	-1	0	-1	0	3	0	-1	0	0	0
03	0	0	0	0	0	0	0	0	0	0	0	0	-1	0	(3)	0	0	-1	0
13	0	0	0	0	0	0	0	0	0	-1	0	0	0	0	0	3	0	-1	-1
23	0	0	0	0	0	0	0	0	0	0	0	0	0	-1	0	0	(3)	0	-1
04'	0	0	0	0	0	0	0	0	0	0	0	0	0	0	-1	-1	0	(3)	0
14'	0	0	0	0	0	0	0	0	0	0	0	0	0	0	0	-1	-1	0	(3)

M2

	20	30	11'	21'	31'	11	31	02'	32'	HOLE	02	32	03'	23'	03	13	23	04'	14'
23C	0	0	0	0	0	0	0	0	0	1	0	0	0	-1	0	0	0	0	0
23B	0	0	0	0	0	0	0	0	0	0	0	0	0	1	0	0	-1	0	0
23A	0	0	0	0	0	0	0	0	0	0	0	0	0	0	0	0	1	0	-1
24C	0	0	0	0	0	0	0	0	0	0	0	0	0	0	0	0	1	0	0

Figure 2   19-Element Hexagonal Array with Missing Central Segment

INV(M1)

	29	39	11*	21*	31*	11	31	62*	32*	H	62	32	63*	27	63	13	23	64*	14*
29	0.46805	0.06908	0.19165	0.21249	0.04576	0.10691	0.05119	0.04576	0.02447	0.08333	0.03035	0.02223	0.04530	0.04221	0.02223	0.04190	0.02107	0.02138	0.02069
30	0.06908	0.46805	0.04576	0.21249	0.19165	0.05119	0.10691	0.02447	0.04576	0.08333	0.02223	0.03035	0.04221	0.04530	0.02107	0.04190	0.02223	0.02069	0.02138
11*	0.19165	0.04576	0.46805	0.10691	0.03035	0.21249	0.04530	0.06908	0.02223	0.08333	0.04576	0.02138	0.05119	0.04190	0.02447	0.04221	0.02069	0.02223	0.02107
21*	0.21249	0.21249	0.10691	0.53055	0.10691	0.10826	0.10826	0.05119	0.05119	0.16667	0.04530	0.04530	0.09473	0.04221	0.08349	0.04190	0.04190	0.04190	0.04190
31*	0.04576	0.19165	0.03035	0.10691	0.46805	0.04530	0.21249	0.02223	0.06908	0.08333	0.02138	0.04576	0.04190	0.05119	0.02069	0.04221	0.02447	0.02107	0.02223
11	0.10691	0.05119	0.21249	0.10826	0.04530	0.53055	0.09473	0.21249	0.04221	0.16667	0.10691	0.04190	0.21249	0.10826	0.08349	0.05119	0.09473	0.04530	0.04221
31	0.05119	0.10691	0.04530	0.10826	0.21249	0.09473	0.53055	0.04221	0.21249	0.16667	0.04190	0.10691	0.08349	0.10826	0.04190	0.09473	0.05119	0.04221	0.04530
62*	0.04576	0.02447	0.06908	0.05119	0.02223	0.21249	0.04221	0.46805	0.02107	0.08333	0.19165	0.02069	0.10691	0.04190	0.04576	0.04530	0.02138	0.03035	0.02223
32*	0.02447	0.04576	0.02223	0.05119	0.06908	0.04221	0.21249	0.02107	0.46805	0.08333	0.02069	0.19165	0.04190	0.10691	0.02138	0.04530	0.04576	0.02223	0.03035
H	0.08333	0.08333	0.08333	0.16667	0.08333	0.16667	0.16667	0.08333	0.08333	0.33333	0.08333	0.08333	0.16667	0.16667	0.08333	0.08333	0.08333	0.08333	0.08333
62	0.03035	0.02223	0.04576	0.04530	0.02138	0.10691	0.04190	0.19165	0.02069	0.08333	0.46805	0.02107	0.21249	0.04221	0.06908	0.05119	0.02223	0.04576	0.02447
32	0.02223	0.03035	0.02138	0.04530	0.04576	0.04190	0.10691	0.02069	0.19165	0.08333	0.02107	0.46805	0.04221	0.21249	0.02223	0.05119	0.06908	0.02447	0.04576
63*	0.04530	0.04221	0.05119	0.09473	0.04190	0.21249	0.08349	0.10691	0.04190	0.16667	0.21249	0.04221	0.53055	0.09473	0.21249	0.10826	0.04530	0.10691	0.05119
27	0.04221	0.04530	0.04190	0.09473	0.05119	0.08349	0.10826	0.04190	0.10691	0.16667	0.04221	0.21249	0.09473	0.53055	0.04530	0.10826	0.21249	0.05119	0.10691
63	0.02223	0.02107	0.02447	0.04221	0.02069	0.04190	0.04576	0.02138	0.03035	0.08333	0.06908	0.02223	0.21249	0.04530	0.46805	0.10826	0.03035	0.19165	0.04576
13	0.04190	0.04190	0.04221	0.08349	0.04221	0.09473	0.09473	0.04530	0.04530	0.16667	0.05119	0.05119	0.10826	0.10826	0.10691	0.53055	0.10691	0.21249	0.21249
23	0.02107	0.02223	0.02069	0.04221	0.02447	0.04190	0.05119	0.02138	0.04576	0.08333	0.02223	0.06908	0.04530	0.21249	0.03035	0.10691	0.46805	0.04576	0.19165
64*	0.02138	0.02069	0.02223	0.04190	0.02107	0.04530	0.04221	0.03035	0.02223	0.08333	0.04576	0.02447	0.10691	0.05119	0.19165	0.21249	0.04576	0.46805	0.06908
14*	0.02069	0.02138	0.02107	0.04190	0.02223	0.04221	0.04530	0.02223	0.03035	0.08333	0.02447	0.04576	0.05119	0.10691	0.04576	0.21249	0.19165	0.06908	0.46805

M2*INV(M1)

|	29	30	11*	21*	31*	11	21	62*	32*	H	62	32	63*	27	63	13	23	64*	14*
23C	0.04112	0.03803	0.04143	0.08194	0.03215	0.08319	0.05841	0.04143	-0.02389	0.16667	0.04112	-0.12915	0.08194	-0.36388	0.03803	0.05841	-0.12915	0.03215	-0.02389
23B	0.02114	0.02309	0.02301	0.04252	0.02672	0.04190	0.05707	0.02052	0.05116	0.08333	0.02042	0.12641	0.31806	0.01495	0.00134	-0.25666	0.00842	-0.00474
23A	0.00009	0.00006	-0.00009	0.00001	0.00224	-0.00031	0.00589	-0.00005	0.01540	0.00000	-0.00224	0.04003	-0.00698	0.10057	-0.01540	-0.10057	0.27639	-0.04003	-0.27639
24C	0.02107	0.02223	0.02069	0.04221	0.02447	0.04190	0.05119	0.02138	0.04576	0.08333	0.02223	0.06908	0.04530	0.21249	0.03035	0.10691	0.46805	0.04576	0.19165
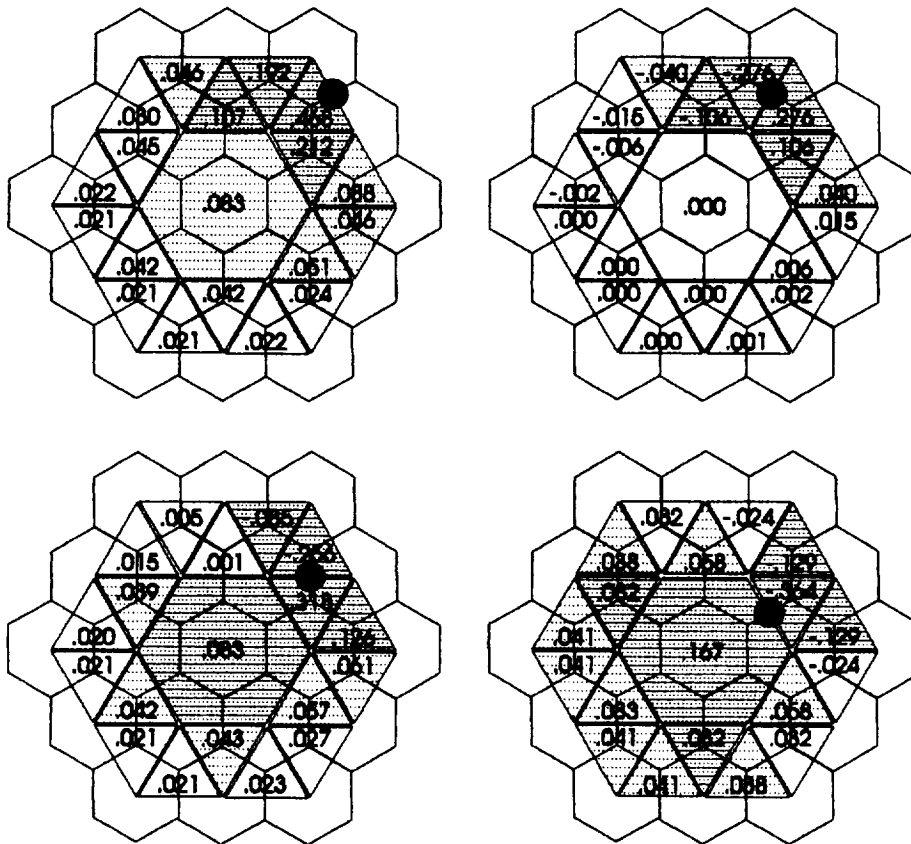
Figure 2a   Solution for 19-Element Hexagonal Array with Missing Central Segment

SOME ASPECTS OF PHOTOVOLTAIC POWER CONVERSION WITH LASER ILLUMINATION

Dr. Glenn W. Zeiders, The Sirius Group

The current-voltage characteristic of a p-n junction photovoltaic converter is given by

$$I = I_{sc} - I_0 (e^{V/V_0} - 1)$$

where I_{sc} is the short-circuit current when the cell is illuminated, and I_0 and $V_0 = nkT/e$ are characteristics of the cell. The parameter n is ideally unity but can be as much as three for real systems, $kT/e = 26$ mV @ room temperature, and the open-circuit voltage $V_{oc} = V_0 \, ln(1 + I_{sc}/I_0)$ is about 550 mV for Si at one sun and rises linearly with bandgap, so I_{sc}/I_0 is generally quite large for cases of interest. Since photon flux is effectively converted to electron flow, the short-circuit current I_{sc} is proportional to the incident radiant intensity. The simplest realistic equivalent circuit for a cell is a current source with a series resistance R_s, so the overall circuit behavior for an array of identical cells with uniform illumination is described by

$$X = ln \{ I_{sc} / I_0 + 1 - Y \} - Y \ (I_0 R_s / V_0)$$

where $X = V/NV_0$ and $Y = I/I_0$ for series-connection of N cells, $X = V/V_0$ and $Y = I/NI_0$ for parallel-connection, and where V and I are the system output voltage and current. The conversion efficiency is proportional to $X\,Y = IV / V_0 I_{sc} N$, and is realized for

$$d \, (X\,Y) / dY = ln \{ I_{sc} / I_0 + 1 - Y \} - Y / \{ I_{sc}/I_0 + 1 - Y \} - 2Y \, (I_0 \, R_s / V_0) = 0,$$
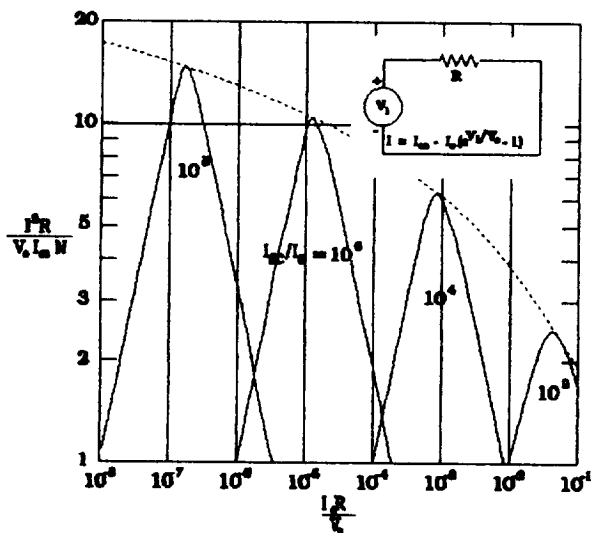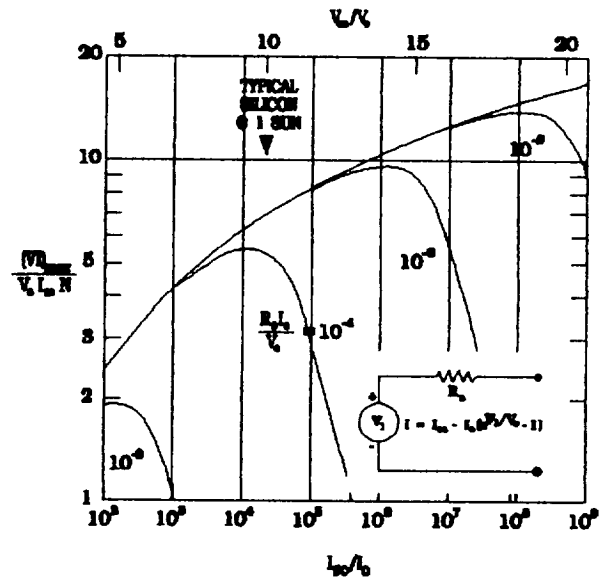

Fig.2 Photovoltaic Response

Fig.1 Peak Photovoltaic Response

the result of which is plotted in Fig. 1. The optimized "efficiency" rises slowly at first because of the logarithmic variation of V_{oc}, but then falls abruptly due to $I^2 R_s$ ohmic heating in the series resistance. Because the optimum current is proportional to the I_{sc} and the optimum voltage is proportional to V_{oc}, the optimum load resistance $R = V / I$ varies roughly

inversely with I_{sc}, so the series resistance becomes more critical at high illumination levels. The effect of the total resistance (load and internal) is shown in Fig. 2, from which it can be seen that a very serious performance penalty is paid if the resistance is not within at least a factor of two of the optimum value. This can easily be handled with solar flux alone, but the required accuracy and dynamic range may be quite difficult to achieve if the system must also accommodate large peak currents from laser pulses.

The problem is further complicated with laser illumination because, unless the array is flood-loaded with the beam, the illumination will vary both spatially (due to the beam intensity profile) and temporally (due to beam wander from system jitter and atmospheric turbulence along the path.) It has been suggested that cells be connected in series to provide high voltage at reduced load current, thereby decreasing the series-resistance loss, but that does not work well when the irradiation varies appreciably over that portion of the array. The impact of the type of connection is shown quite effectively in Fig. 3 with a simple two-cell example for which series and parallel connections are compared with both matched and unmatched cells. Internal resistances are neglected in the figure, and it is assumed in the latter case that the weaker cell has half the illumination of the other ($I_{sc}/I_0 = 2 \cdot 10^6$ for the higher.) Load lines are shown for optimum operation with the matched cells, and, while the total incident power decreases to 75% for the unmatched case, the electrical power with series connection drops to 31% whereas it falls only to 71% with parallel connection. The reason for the nearly constant efficiency with parallel connection is that the open-circuit voltage will be changed little by mismatching (again because of the weak logarithmic dependence on ΣI_{sc}), and the total current will continue to be near the sum of the individual short-circuit currents. On the other hand, the maximum current with series connection will be no more than about the short-circuit current of the weakest cell, and that cell's open circuit voltage will depend on it's short-circuit current alone, so the efficiency can be dramatically reduced by mismatch-

Fig. 3 Effect of Cell Connection

ing as found in the example. In the worst case of complete "shadowing", weakly-irradiated cells in series not only decrease performance, but they can also act as dead shorts capable of causing severe damage through "hot-spot" formation. Diodes can be used to protect against such damage, but they do not overcome the performance loss, and they add weight and complexity to the system; some protection is afforded as well by leakage currents arising from defects and edge effects in the cells, but their effect is generally unimportant otherwise. The net effect of this is that series connection can -- and probably should -- be used over regions small compared to the instantaneous size of the main beam in order to obtain the desired voltage while reducing series resistance loss, but these elements should then be either independent or connected in parallel to maximize efficiency over regions with significant intensity variation.
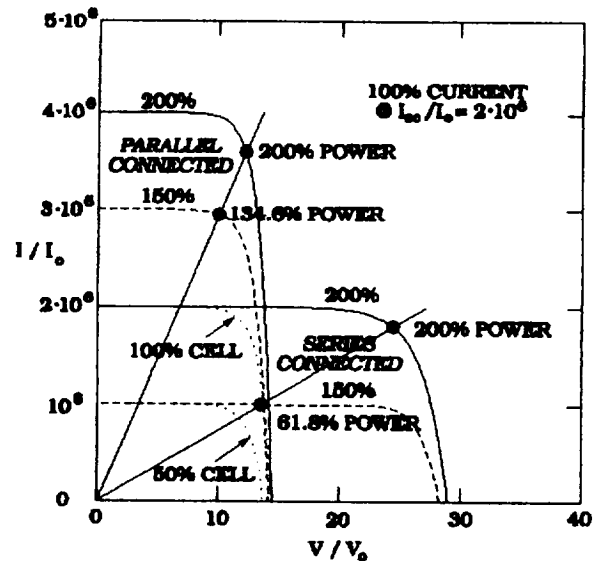
The response to a directed beam (especially one from the free-electron laser of interest for power beaming) can be modeled by assuming a gaussian distribution of intensity and, in view of the above results, a system of individual elements each with its own load resistance. Neglecting internal losses, the converted power distribution is

$$P'(r) = 2\pi \int_0^r I^2 R\, r\, dr \quad \text{where} \quad \exp(IR/V_0) - 1 + I/I_0 = (I_{sc}/I_0)_{max} \exp(-r^2/2a^2),$$

Case I: $R = $ constant or Case II: $I/I_0 = (V_0/I_0 R)\, ln\, (V_0/I_0 R)$ for local optimization,

and where R is the resistance per unit area of the array. The total power output for the two cases (again normalized with respect to I_{sc} to represent "efficiency") is shown in Fig. 4; the maximum power output with uniform resistive loading and gaussian illumination is achieved if the load is optimized for about 55% of the peak short-circuit current, and the performance penalty for not using locally-optimized loading is 27% at $I_{sc}/I_0 = 10^8$ and improves to 15% at 10^3. This rather nominal performance penalty with fixed loading may, indeed, prove to be a very small price to pay when one considers that the locally-optimized loading would have to be "active" at relatively high frequencies to account for centroid motion; the constant-resistance
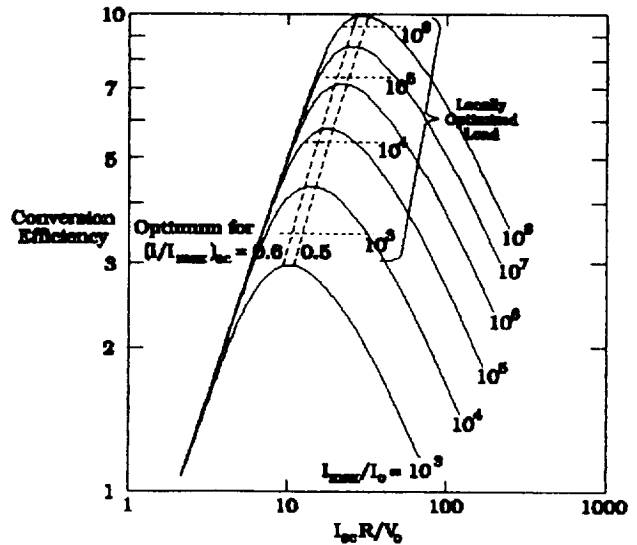

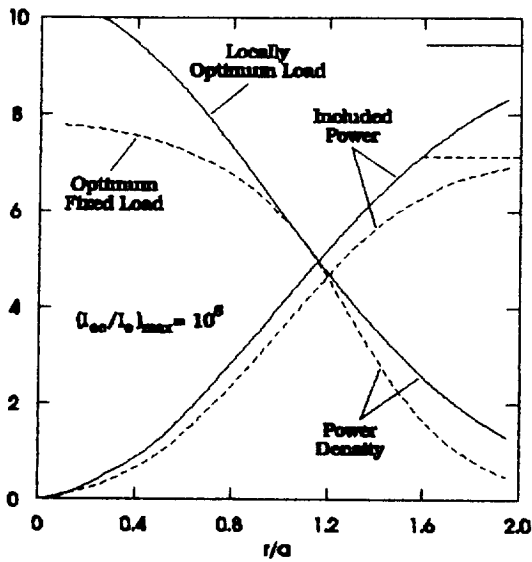**Fig. 4 Photovoltaic Response to Gaussian Irradiation**

"passive" load might have to be variable as well (particularly for space vehicles) to account for changes of peak intensity, but those variations would be applied on a global scale at much lower frequencies. Fig. 5 shows the distribution of output power density and included power for $(I_{sc}/I_0)_{max} = 10^6$ for the optimum fixed resistance as well as for locally-optimized ("active") loading. The value of the fixed resistance is higher than optimum in the high-intensity central region and lower than optimum in the wings, but the penalty is rather nominal as noted earlier, and the output distribution is somewhat compressed. For example, 86.5% of the incident power is included within the $1/e^2$ radius r = 2a, whereas, for the case shown in Fig. 5, that same fraction of the output power is included within r/a = 1.89 with local optimization and only 1.55 with the optimum constant load, thereby providing the possibility of a smaller receiver.

Fig. 5 Distribution of Optimized Response to Gaussian Irradiation

REPORT DOCUMENTATION PAGE

Form Approved
OMB No. 0704-0188

Public reporting burden for this collection of information is estimated to average 1 hour per response, including the time for reviewing instructions, searching existing data sources, gathering and maintaining the data needed, and completing and reviewing the collection of information. Send comments regarding this burden estimate or any other aspect of this collection of information,including suggestions for reducing this burden, to Washington Headquarters Services,Directorate for Information Operations and Reports,1215 Jefferson Davis Highway, Suite 1254, Arlington VA 22202-4302, and to the Office of Management and Budget, Paperwork Reduction Project (0704-0188), Washington DC 20503.

1. AGENCY USE ONLY (Leave blank)	2. REPORT DATE 7 May 93	3. REPORT TYPE AND DATES COVERED Final Report for 5 May 92 - 30 Oct 92

4. TITLE AND SUBTITLE Laser Beamed Power Systems Analysis	5. FUNDING NUMBERS NASA/MSFC H-11986D 1-2-PP-02176 (F)

6. AUTHOR(S)

Dr. Glenn W. Zeiders Jr.

7. PERFORMING ORGANIZATION NAME(S) AND ADDRESS(ES) The Sirius Group 227 Bartholomew Street Peabody, Massachusetts 01960	8. PERFORMING ORGANIZATION REPORT NUMBER

9. SPONSORING / MONITORING AGENCY NAME(S) AND ADDRESS(ES) George C. Marshall Space Flight Center Marshall Space Flight Center, Alabama 35812	10. SPONSORING / MONITORING AGENCY REPORT NUMBER

11. SUPPLEMENTARY NOTES

12A. DISTRIBUTION/ AVAILABILITY STATEMENT Unlimited	12b. DISTRIBUTION CODE

13. ABSTRACT (Maximum 200 words)

The NASA SELENE power beaming program is intended to supply cost-effective power to space assets via Earth-based lasers and active optics systems. Key elements of the program are analyzed, the overall effort is reviewed, and recommendations are presented.

14. SUBJECT TERMS space power, power beaming, lasers, adaptive optics	15. NUMBER OF PAGES 42
	16. PRICE CODE

17. SECURITY CLASSIFICATION OF REPORT Unclassified	18. SECURITY CLASSIFICATION OF THIS PAGE Unclassified	19. SECURITY CLASSIFICATION OF ABSTRACT Unclassified	20. LIMITATION OF ABSTRACT None

NSN 7540-01-280-5500

Standard Form 298 (Rev. 2-89)
Prescribed by ANSI Std. 239-18
298-102